A method to update model kinematic states by assimilating satellite-observed total lightning data to improve convective analysis and forecasting

Zhixiong Chen[1, 2], **Xiushu Qie**[1, 2],

1. Key Laboratory of Middle Atmosphere and Global Environment Observation (LAGEO), Institute of Atmospheric Physics, Chinese Academy of Sciences, Beijing, China

2. College of Earth and Planetary Science, University of Chinese Academy of Sciences, Beijing, China

Juanzhen Sun[3], **Ying Zhang**[3], **Zhuming Ying**[3]

3. National Center for Atmospheric Research, Boulder, Colorado, USA

Xian Xiao[4]

4. Beijing Urban Meteorological Engineering Research Center, Beijing, China

Dongjie Cao[5]

5. National Satellite Meteorological Center, Beijing, China

Corresponding author:

Dr. Xiushu Qie

Email: qiex@mail.iap.ac.cn

Tel: +86-010-82995091

Fax: +86-010-82995073

Key Points:

- A lightning data assimilation (DA) scheme to update model kinematic states was developed using a three-dimensional variational (3DVar) system.
- The Event data from Lightning Mapping Imager (LMI) aboard the FY-4A geostationary satellite were assimilated to reflect lightning horizontal dimension.
- The new lightning DA scheme improves the convective analysis and storm forecasting in two severe convective cases.

Abstract: The close connection between the total lightning flash rate and storm updraft has been well recognized. In this study, we assessed the benefit of such a relationship in convective-scale data assimilation (DA) for model initialization. A lightning DA scheme to update model kinematic states was developed in the Weather Research and Forecasting Data Assimilation (WRFDA) three-dimensional variational (3DVar) system. This scheme combines total lightning observations with model-based prescribed vertical velocity profiles to retrieve kinematic information useful to DA. With the availability of space-borne lightning imagers in recent years, total lightning data observations from the Lightning Mapping Imager (LMI) on board the FY-4A geostationary satellite were assimilated in combination with radar DA. A detailed analysis of the impact of the lightning DA scheme on convective precipitation forecasting was conducted using a squall line case over Beijing on 13 July 2017. The results showed that the assimilation of LMI data further improves the analyses of dynamical conditions from assimilating radar radial winds. Although the microphysical states are identical due to the assimilation of reflectivity, updrafts directly form at lightning observation locations via lightning DA and hence improve the convective-scale dynamical balance. The quantitative verification of short-term convective forecasts indicated that the lightning DA adds value to current radar DA by improving the precipitation forecast skill. The new lightning DA scheme was further applied to a heavy rainfall case in 2018, and the results confirmed the effective and robust improvement in storm forecasting.

Plain Language Summary: Lightning flashes are closely related to the upward air motions in thunderstorms, and hence are indicative of strong wind convergence. Currently, lightning imagers on board the geostationary satellites provide increased availability of lightning data over broad regions and can improve weather forecasting accuracy. This paper describes how the space-borne lightning observations could be employed to update model kinematic states and improve convective precipitation forecasting.

1. Introduction

Radar observations, including radial velocity, reflectivity and polarimetric observations, are the primary source of data that provide convective information with a high spatiotemporal resolution. The assimilation of these data can effectively update the dynamical and microphysical states, resulting in an improvement in high-impact weather forecasting (see Sun et al. 2014 and Gustafsson et al. 2018 for relevant reviews). However, the positive impact is highly dependent on the quality of the radar observations and the methodology used to assimilate the convective information obtained from those observations. Although radar networks have been built and are operationally used in many countries, there are still many wide gaps in their spatial coverage. In addition, it is particularly challenging for weather radar to acquire observations over mountainous regions, where emitted radar beams suffer from full or partial terrain blocking. Thus, efforts have been made to combine radar data assimilation (DA) with other data sources, such as lightning observations provided by traditional ground-based lightning detection networks (Fierro et al. 2012, 2014; Chen et al. 2019). In recent years, lightning imagers aboard geostationary satellites have become available, for example, the Geostationary Lightning Imager (GLM) on the GOES-R satellite and the Lightning Mapping Imager (LMI) on the FY-4A satellite. These space-borne lightning detectors continuously observe the total lightning flashes [i.e., cloud-to-ground (CG) plus intracloud (IC) lightning] over both the continents and the oceans with a spatial resolution of kilometers, and these observations complement the existing radar networks in the monitoring of severe storms. The effective assimilation of space-borne lightning data, especially when combined with radar observations, is expected to improve short-term convective forecasts.

Lightning activities are believed to be electrical responses of thunderstorm evolution. The widely accepted noninductive charging (NIC) theory states that the primary source of charge separation is the rebounding collisions between graupel and

ice crystals in the presence of supercooled liquid water. Accordingly, NIC theory lays the physical basis for assimilating lightning observations. For example, the state variables retrieved from lightning flash rates via empirical relationships, such as latent heat (Alexander et al. 1999; Pessi et al. 2009), specific humidity (Papadopoulos et al. 2005; Mansell et al. 2007; Fierro et al. 2012, 2014, 2015, 2016, 2019; Zhang et al. 2017; Hu et al. 2020), hydrometer mass (Qie et al. 2014; Mansell et al. 2014; Wang et al. 2017; Chen et al. 2019; Kong et al. 2020) and temperature (Marchand et al. 2015), are assimilated to force the convection at locations where lightning is observed. Generally, these lightning DA methods are very similar to the methods used to assimilate radar reflectivity observations that force convection by adjusting the microphysical or thermodynamic state variables. For example, when lightning flash rates exceed a specified threshold, derived moisture is assimilated into model using variational DA technique (e.g. Fierro et al. 2016, 2019; Hu et al. 2020), which induces buoyancy-generated lifting from positive adjustments of water vapor mixing ratios, in a similar fashion to moisture adjustment based on radar reflectivity (Wang et al. 2013a). However, unlike radar networks from which kinematic information is provided by radial velocity observations, lightning observations do not directly provide kinematic information. Since it has been shown that the kinematic information can help alleviate model spin-up problem when combined with reflectivity assimilation and improve dynamical balance (Xiao and Sun, 2007; Sun 2005), in this study, we explore the possibility to update model kinematic states from lightning observations and the resulting benefit on convective forecasting.

Relationships between the total lightning flash rate and strong updrafts in deep convection have been proposed through field observations and numerical studies. According to NIC theory, strong updrafts are required to support the production of supercooled water and suspend graupel particles, which are necessary for storm electrification. Deierling and Petersen (2008) analyzed the total lightning flash rate and the updraft volume associated with the vertical velocities w >5 m s^{-1} and w >10 m

119 s^{-1} above the freezing level, and they found a strong linear correlation between them.
120 In the numerical studies of electrification and lightning by Kuhlman et al. (2006), it
121 was also shown that the total lightning flash rate is well correlated with the updraft
122 volume and updraft mass flux. Considering the importance of updrafts on cloud
123 electrification and lightning, the maximum updraft velocity (w_{max}) is employed in the
124 lightning parameterization scheme of Price and Rind (1992, hereafter PR92) to
125 diagnose the lightning flash rate. Since the lightning flash rate is closely associated
126 with the strength of storm updrafts, lightning flashes are theoretically indicative of
127 regions with strong upward air motions and hence significant low-level convergence.
128 If the updraft information provided by lightning data is introduced into a model, it is
129 possible to update the 3-dimensional wind components at lightning observation
130 locations via the continuity equation. As a result, air parcels are more likely to reach
131 their level of free convection (LFC) to form convection due to enhanced uplift from
132 the updated kinematic states. From this perspective, using lightning data to directly
133 update model kinematic states can be more physically effective than forcing
134 convection by inserting water vapor and/or hydrometeors.

135 The strong connection between the total lightning flash rate and storm updraft
136 implies that total lightning flashes are indicative of the updraft intensity and the
137 timing of convective development (MacGorman et al. 1989; Schultz et al. 2011;
138 Fierro et al. 2012). Currently, lightning detectors aboard geostationary satellites are
139 capable of obtaining wide-range observations of total lightning activities and hence
140 present an opportunity to assess the impact of lightning observations on model
141 kinematic variables and convective forecasting. The greatest challenge in fully
142 exploiting the kinematic information contained in total lightning activity observations
143 is developing a reliable observation operator in the DA context. In the PR92 lightning
144 parameterization scheme, a simple formula estimating the total lightning flash rate
145 from w_{max} was proposed, which provided a basis for deriving w_{max} from the observed
146 lightning flash rate. However, it is challenging to assimilate lightning-derived w_{max}

information. The two-dimensional w_{max} field lacks height information, which means that the vertical location of the strongest updraft in a column is not known. Finally, space-borne lightning detections usually have poorer resolutions than lightning observations from ground-based networks. The typical resolution of a lightning imager (e.g., LMI) equipped on a geostationary satellite is coarser than that of the present-day convection-permitting models (1-4 km).

In this study, we propose a scheme that aims to improve the analysis of model kinematic states by the assimilation of total lightning observations from the LMI on board the FY-4A geostationary satellite with a three-dimensional variational (3DVar) DA system. Although the scheme is not limited to any particular DA technique, we use the 3DVar system for implementation and testing mainly due to its widespread operational applications and lower computational costs. In this scheme, pseudo-vertical velocity observations are obtained by combining lightning-derived w_{max} information with prescribed model-based vertical profiles depicting the vertical distribution of the vertical velocity w. Then, an observation operator for horizontal convergence is developed in the 3DVar cost function. To address the issue of the LMI sampling resolution, we present a data preprocessing procedure to generate input data compatible with numerical weather prediction (NWP) models while minimizing the loss of information contained in the LMI lightning data. Considering the proven role of radar observations in convective-scale data assimilation, we evaluate the benefit of the kinematic information derived from the total lightning observations in addition to radar DA. Therefore, the combined assimilation of radar and lightning data is conducted, and the results are compared with those of experiments assimilating either data type alone. We first show a set of single observation tests to illustrate the effects of assimilating these two types of data on analysis increments. The real data impact of the kinematic-based lightning DA scheme with and without radar DA is evaluated by two convective cases with heavy precipitation. The impact of LMI data preprocessing on the DA and subsequent forecasting is assessed via sensitivity experiments.

The rest of this paper is organized as follows. Section 2 describes both the processing method for total lightning data from the LMI suitable for the purpose of convective-scale DA and the Weather Research and Forecasting Model Data Assimilation (WRFDA) 3DVar and forecast system. In Section 3, the LMI lightning DA scheme in the 3DVar system is described in detail. The results of single observation tests and real case studies are presented in Section 4 and Section 5, respectively. Our conclusions are summarized in Section 6.

2. Description of the data, WRFDA 3DVar, and forecast system

Both conventional observations from the GTS (Global Transmission System) and unconventional observations are used in this study. The unconventional data include radial velocity and reflectivity observations from a network of six operational Doppler radars in a region of North China surrounding Beijing (Fig. 1) and from the LMI on board the FY-4A geostationary satellite. The radar observations have been operationally assimilated in WRFDA 3DVar by the Beijing Meteorological Service since 2012. The reader is referred to Chen et al. (2012; 2014) for a detailed description regarding the preprocessing and quality control (QC) of the Beijing radar network. Due to the complex terrain in this region with high mountains in the northwest and the Bohai Bay in the southeast, the radar network suffers from topographic blocking in the mountainous area. In this paper, our main focus is space-borne LMI total lightning data, whose preprocessing and QC are described below. The DA system and WRF model will be described later in this section.

Fig. 1

a. Preprocessing of the LMI data

The LMI on board the FY-4A geostationary satellite that was launched successfully in December 2016 is the first satellite-based lightning detector in China. Different from ground-based lightning location systems, the LMI observes the optical

evolution of lightning flashes instead of changes in the electrical field. A 400×600 charge coupled device (CCD) array plane is adopted to detect changes in brightness at cloud tops induced by lightning flashes over China and its adjacent oceanic regions (Cao et al. 2018; Hui et al. 2020). The LMI observes lightning flashes at a rate of 500 frames per second with a pixel resolution of 7.8 km at the subsatellite point. In each frame, if a pixel is illuminated by lightning, it is termed an event with the pixel centroid as its latitude-longitude coordinates. The lightning event product is the basic LMI detection element, and events can be further combined into group and flash products using a lightning clustering algorithm (Christian et al. 1999; Mach et al. 2007; Goodman et al. 2013).

Since the LMI tracks the brightness changes at cloud tops, the instrument detects the total lightning flashes without discriminating between IC and CG lightning flashes, and its three product levels, including the event, group and flash products, are capable of resolving storm updraft characteristics. In this study, the LMI event product is employed instead of the group and flash products for two reasons. First, the LMI event product records all lightning-illuminated pixels, which can better depict the spatial propagation of lightning flashes and, hence, convective regions (Peterson, 2019). Since the flash and group products are collections of lightning events satisfying some prespecified temporal and spatial thresholds, some of the information on the storm location, coverage and intensity can be lost. Second, the values of the group and flash products are greatly impacted by the lightning clustering algorithm applied. Therefore, using the event product can avoid the uncertainties originating from lightning clustering algorithms.

For the purpose of DA, a quality control procedure should not only remove unreliable observations but also define the observation error (measurement plus representative error) for the “good” observations. For the instantaneous point measurements of the LMI, however, it is difficult to estimate such observation errors quantitatively. Alternatively, we preprocess the LMI data by the so-called

scale-matching approach (Janjic et al. 2017); i.e., we filter out the high-frequency scales in the observations such that the data to be assimilated match the resolvable scales of the numerical model used for the data assimilation. Specifically, the QC procedure implemented in this study includes the following three steps:

(1) Remove isolated event data with no adjacent illuminated pixels. These isolated data are removed because they are typically regarded as noise.

(2) Temporally bin the LMI event data. The quality-controlled lightning event data are binned into 15-min time periods from the original level-II 1-min data provided by the National Satellite Meteorological Center, Chinese Meteorological Administration.

(3) Spatially regrid the LMI event data to the model grid, as illustrated in Fig. 2. Because the LMI pixel resolution is approximately 7.8 km, in the context of DA at the convective scale (<3 km), a 5-km search radius is applied to count the number of lightning events at each model grid. To be more specific, provided with the WRF model Cartesian grid coordinates and the binned 15-min LMI events, the number of lightning events that occurred within a 5-km radius of each grid are summed and termed the LMI event density (LED). The regridded LED with a 5-km radius is able to maintain the compactness of lightning occurrences. Following the idea behind PR92, stronger updrafts (w_{max}) are expected over regions with higher LED. The values of w_{max} and the corresponding ranges of LED will be described in the next section.

While it is not common practice to regrid observation data to model grids in DA for other types of observations, such as radiosondes, we believe this approach is an appropriate practice for space-borne lightning data. Most DA schemes assume a Gaussian distribution for the background error covariance, which implies that the observation information is spread out among grid points devoid of observations according to Gaussian statistics. Lightning flashes apparently violate the Gaussian error assumption because they are confined to electrically active regions within thunderstorms.

Fig. 2

Since the LMI detects the brightness changes at cloud tops, the detection efficiency and accuracy can be influenced by the cloud depth and optical diffusion due to the spreading of optical pulses. Consequently, lightning flashes propagating through optically thick clouds could be underestimated or undetected. However, accurately estimating the underestimation by thick clouds is a complicated research topic deserving a separate investigation, and is beyond the scope of the current study and thus is not considered here.

b. **WRFDA 3DVar and forecast system**

The 3DVar method is widely used at operational NWP centers, especially for regional models, because of its low computational cost and fewer technical difficulties associated with nonlinearities. In this study, the WRFDA 3DVar system (Version 3.9.1) is applied. WRFDA 3DVar is able to assimilate radar radial velocity (Xiao and Sun, 2007) and reflectivity observations (Wang et al. 2013a; Tong et al. 2016; Gao et al. 2018) as well as conventional observations. A new observational term associated with lightning-derived kinematic data is incorporated into the total cost function of 3DVar as follows:

$$J = J_b + J_{obs} + J^{V_r}_{radar} + J^{q_v}_{radar} + J^{q_r}_{radar} + J^{w}_{lightning}, \qquad \textbf{(1)}$$

where J_b stands for the background term defined by the analysis departure from a WRF forecast, J_{obs} stands for the conventional observation term measuring the analysis departure from conventional observations, and the three terms with the "radar" subscript are the observation terms corresponding to the radial velocity, pseudo-in-cloud humidity and hydrometeors retrieved from reflectivity observations. The last term is the observation term for the pseudo-kinematic observations derived from the lightning data, which will be introduced in detail in the next section. By minimizing the total cost function *J*, WRFDA 3DVar seeks an optimal initial state

between the background field and observations to drive the WRF model forecast. In this study, the WRFDA 3DVar system utilizes climatological background error statistics to represent the uncertainty of the model forecast background. Provided with 24-h and 12-h WRF forecasts for the month of July 2017, the background error statistics were generated following the National Meteorological Center (NMC) method (Parrish and Derber, 1992) by the WRFDA 3DVar tool GEN_BE (Barker et al. 2004). The control variable option CV7 was used, which employs the following control variables: x- and y-component winds (*u* and *v*, respectively), temperature (*T*), surface pressure (*Ps*), relative humidity (*RH*), and hydrometeors (*Qr*, *Qs*, and *Qg*). According to Sun et al. (2016), the *u/v* momentum control variables allow closer fits to high-resolution observations than allowed by traditional stream function/velocity potential control variables.

All the numerical experiments in this study employ a two-way, three-domain nested grid using the WRF model. The outermost domain has 650×650 grids with a 9-km horizontal grid spacing, while the inner and innermost domains both have 1060×1060 grids with 3-km and 1-km horizontal grid spacings, respectively. The number of terrain-following vertical levels is set to 45, and the model top is set to ~50 hPa. The model physics options include the Kain-Fritsch cumulus parameterization scheme (Kain and Frisch, 1993), which is applied only to the outermost domain, the NSSL 2-moment bulk microphysics scheme (Mansell et al. 2010), the Bougeault-Lacarrère PBL scheme (Bougeault and Lacarrere, 1989), the Noah land surface model (Chen and Dudhia, 2001), the RRTM scheme (Mlawer et al. 1997) and the Dudhia scheme (Dudhia, 1989) for longwave and shortwave radiation processes.

WRFDA 3DVar is used to initialize the WRF model forecast by assimilating conventional observations, including radiosonde, surface network and aircraft data, as well as high-resolution radar and lightning observations. To effectively extract information from observations with different spatiotemporal scales, the two-step DA strategy designed for WRFDA (Tong et al. 2016) is applied. In the first step,

conventional observations are assimilated with Global Forecast System (GFS) data as the background first guess. Then, the model forecasts from the first step are used as the background, and a shorter length scale and analysis cycle are applied to assimilate the radar and lightning data in the second step.

3. The lightning data assimilation method

a. Method to estimate w_{max}

Following the idea of the PR92 lightning parameterization scheme (Price and Rind, 1992), we first obtain the magnitude of the column-maximum updraft w_{max}, derived from the total lightning observations (e.g., LED). By examining the cumulative distributions of the 15-min binned LED data (Fig. 3), we found that the most frequent values of the event density are below 20 events per 15 min and account for approximately 80% of the entire LED range. Based on the results in Fig. 3, the ranges of the 60th, 80th and 90th percentile event densities are used to determine the magnitudes of the maximum vertical velocity w_{max} (Table 1). The procedure employed to determine the value of w_{max} for each of the LED ranges is described below.

Fig. 3

While the correlation between the lightning flash rate and column-maximum vertical velocity w_{max} has been confirmed by previous studies, the quantitative determination of w_{max} is not straightforward. PR92 found that the minimum w_{max} is 14.7 m s^{-1} once lightning flashes occur based on their calculations. Moreover, according to field observations (e.g., Zipser and Lutz, 1994), a mean vertical velocity of 6 m s^{-1} was necessary to facilitate significant cloud electrification and initiate lightning. Based on these findings, the upper and lower limits for the values of w_{max} are set to 15 m s^{-1} and 5 m s^{-1}, respectively, for the ranges of the 60th, 80th and 90th percentile event densities with an incremental interval of 3~4 m s^{-1} (see Table 1), which is the uncertainty magnitude of vertical velocity profiles shown in the next

section. Although larger values of w_{max} were observed in electrified convection (e.g., Calhoun et al. 2013), we set this upper limit because larger values are not resolvable by the model (in terms of the accuracies of both the value and the location) and hence can be easily rejected by the WRFDA innovation check.

Table 1

b. Prescribed vertical velocity profile

Since w_{max} does not include information about its vertical location, a key step in the assimilation of w_{max} is to supplement the information of the updraft vertical distribution. Yuter and Houze (1995) analyzed the vertical profile of w over convective areas and found that the updraft typically increases from a low value at low levels to a peak value at the middle to upper levels and then decreases in value toward the top of the storm. For the purpose of the present study, we believe that an ensemble of model forecasts is most suitable for estimating the vertical velocity w profile. The same model forecasts of July 2017 generated for the calculation of the background error statistics using the NMC method were used as the ensemble for the w profile estimation. The mean vertical profile was computed by extracting and averaging all the w fields over the convective regions in the model forecasts for the month of July 2017.

In this study, the maximum updraft intensity (up_{max}) and maximum graupel mixing ratio (qg_{max}) in a model column were chosen as the metrics denoting convective regions. Four convective scenarios were designed with up_{max} over 10 m s^{-1} and 15 m s^{-1} corresponding to convective regions with intense updrafts and qg_{max} over 5 g kg^{-1} and 7 g kg^{-1} relating to well electrified convective regions. After the four averaged profiles from these four scenarios were obtained, they were normalized (divided by their respective vertical maxima) and further averaged to obtain the final average profile (Fig. 4a). The model-based profile by this means is generally consistent with the observations of Yuter and Houze (1995) but is more representative

of the updraft characteristics at the time of DA.

With the normalized *w* profile from the model and the w_{max} derived from the lightning flash observations, a 3-dimensional pseudo-*w* observation field can be created by multiplying the two variables at each grid point. It is noted from Fig. 4a that the five profiles differ in the height of the strongest updraft and in the *w* magnitude, especially at lower altitudes, providing different pseudo-*w* observations. The impact of these different prescribed *w* profiles on forecasts will be examined later through sensitivity experiments.

c. Observation operator for lightning DA

The pseudo-*w* observations can be assimilated by adding a vertical velocity observation term to the 3DVar cost function. However, the direct assimilation of *w* may result in excessive noise because there are no constraints or other sources of *w* observations to curb the generation of noise during the data assimilation. Instead, the lightning-derived *w* fields are converted into pseudo-observations of horizontal wind convergence (CON) through the mass continuity equation:

$$CON = \frac{\partial u}{\partial x} + \frac{\partial v}{\partial y} = -\frac{\partial w}{\partial z}, \qquad \textbf{(2)}$$

The CON derived from the pseudo-*w* observations is then assimilated to update the model horizontal wind components *u* and *v* through the following observation term added to the total cost function:

$$J^{w}_{lightning} = \frac{1}{2}\lambda\sum(CON^{mod} - CON^{obs})^2 / \sigma^2_{con} = \frac{1}{2}\lambda\sum((\frac{\partial u}{\partial x} + \frac{\partial v}{\partial y})^{mod} + (\frac{\partial w}{\partial z})^{obs})^2 / \sigma^2_{con}, \qquad \textbf{(3)}$$

where CON^{mod} and CON^{obs} represent the horizontal wind convergence from the model background and its pseudo-observations obtained from the lightning-derived *w* fields, respectively, λ is a weighting coefficient controlling the contribution of the lightning-derived kinematic observational term to the total cost function *J*, and σ^2_{con} stands for the observation error variance of CON.

Fig. 4b shows the calculated CON profiles from the normalized *w* profiles assuming w_{max} = 15 m s^{-1}. These profiles are in good agreement with those from

observations (e.g., Mapes and Lin, 2005; Deshpande et al. 2015), which exhibit low- to middle-level wind convergence and upper-level divergence in storms. Since the horizontal wind convergence influences condensation and precipitation inside storms and is strongly related to the heating profile (Houze 1982; Jonshon, 1984; Mapes and Houze, 1995; Mapes and Lin; 2005), the assimilation of CON profiles could result in enhanced dynamical lifting for air parcels, which would in turn improve the latent heating profiles.

To estimate the uncertainty of the *w* profiles, we used an ensemble of 35 members produced by setting the values of w_{max} to 5, 8, 11, …, 23 m s^{-1} for each of the five model-based *w* profiles and for the corresponding CON profile via the mass continuity equation. Fig. 4c shows the vertical distributions of the standard deviation and mean of the CON computed from the ensemble. The value of the standard deviation varies within $0.8\sim1.7\times10^{-3}$ s^{-1} at different vertical levels. We found that considering the vertical variation in the uncertainty does not result in an improved assimilation performance; therefore, in the experiments presented, we simply set the observation error σ_{con} for the CON pseudo-observations to a constant value of 1.5×10^{-3} s^{-1}. Single observation experiments using observation errors of $1\sim2\times10^{-3}$ s^{-1} indicated that the resulting analysis increments are not sensitive within this error range (not shown). Hence, the CON pseudo-observations above the maximum *w* level were not used to avoid overfitting the observations.

Fig. 4

4. Single observation tests

Because the CON pseudo-observations obtained from lightning-derived *w* fields are a new type of data in WRFDA, single observation tests were carried out to examine the spread of observations by analyzing the background error statistics and

the responses of the analysis increments to the new observation operator. Three single observation tests were conducted. The test named RA assimilates only the single radial velocity observation. The LN test assimilates only the single LMI lightning observation using the procedure described in the last section. In the RALN test, both the lightning-derived convergence observation and the radial wind observation are simultaneously assimilated. The single radial wind velocity observation is provided by the Doppler radar located at (39.8°N, 116.5°E) in Beijing, and the single CON pseudo-observation is derived from LMI lightning products using the prescribed *w* profiles described above. These single observations are located at the 11th model level (approximately 700 hPa) at (40.4°N, 115.9°E). The observation errors of radial velocity and convergence are set to 1 m s^{-1} and 1.5×10^{-3} s^{-1}, respectively.

Table 2

Table 2 lists the employed value of single observations and corresponding innovation (omb) and residual (oma) terms at the observation location for the three single observation tests. The analysis increments of the horizontal wind field and corresponding convergence at 700 hPa are shown in Fig. 5. In the RA test, because the radial velocity is underestimated in the first guess (-4.544 m s^{-1}), assimilating the single radial wind observation increases the magnitude of the wind speed in the radial direction (Fig. 5a). Note that the spreading distance of the wind increment is determined by the length scale in the background error statistics. The maximum wind increment is approximately 2.6 m s^{-1}, and the residual of the radial wind at the observation location is -0.493 m s^{-1}. In LN, assimilating the CON pseudo-observation successfully enhances the convergence of wind toward the observation location (Fig. 5b); the maximum wind increment is approximately 0.35 m s^{-1}, which is much weaker than that in RA, and the residual of the convergence at the observation location is -0.589×10^{-3} s^{-1}. In RALN, by assimilating both types of observations, not only the wind speed convergence but also the directional convergence are analyzed (Fig. 5c);

as a result, the wind convergence increments are further enhanced from those of RA. Compared with the RA test, the residual of the radial velocity at the observation location in RALN is further reduced, as shown in Table 2, suggesting that the analysis wind fields are closer to the observations by combining radar and lightning DA. The above single observation tests indicate that the combination of radial velocity and lightning-derived convergence observations effectively increases the convergence of wind and reduces the error between the observations and model background.

Fig. 5

5. Real case studies

Using the two-step data assimilation procedure described in Section 2, the radar and lightning observations were assimilated in the second step of our two-step assimilation experiments. In the baseline experiment, RA, we assimilated reflectivity and radial velocity observations from the six radar stations shown in Fig. 1. In the LN experiment, only the pseudo-kinematic observations derived from LMI total lightning data were assimilated. In the RALN experiment, both the lightning-derived convergence observations and the radar observations were simultaneously assimilated to show the value added by assimilating lightning data in addition to the current radar network. Additionally, a control experiment (denoted CTL) was also conducted by assimilating neither radar nor lightning observations, only GTS conventional data. These experiments were conducted using a squall line case with heavy precipitation that occurred over Beijing on 13 July 2017 during the first warm season observing period of LMI launched in late 2016. The results of these experiments are verified and analyzed in detail to demonstrate the impact of the LMI lightning DA on the convective analysis and forecast. To confirm the positive impact of this new scheme, the improvement of another severe rainfall event forecast during the 2018 warm season is also presented.

a. Impact of lightning DA on precipitation forecasting

A squall line convective system occurred in southwestern Beijing on 13 July 2017. The convective cells initiated at approximately 1700 LST (local standard time, = UTC+8 h) and then developed and merged into a squall line by 2000 (Fig. 6a), with its eastern section propagating into the populated area in Beijing. After 2100, the squall line gradually took the shape of bow echoes and then started to break down. The total lightning observations from the LMI in this case provide valuable supplementary convective information in addition to the local radar network (referred to Fig. 1). As shown in Fig. 6b, the distribution of the 15-min binned LED at 2000 shows good agreement with the cloudy regions in the radar reflectivity data since the area with reflectivity greater than 25 dBZ, which is the threshold reflectivity value indicating near saturation in radar DA, exhibits large overlap with the region with an event density greater than 2.

Fig. 6

Since accurate short-term heavy precipitation forecasting is a major concern in NWP, before presenting the impact of the new lightning DA scheme on the analysis of dynamical variables, we first examine the impact of this scheme on the performance of hourly precipitation forecasting through a verification against the hourly radar quantitative precipitation estimate (QPE) produced operationally by the Beijing Meteorology Bureau. The fractions skill score (FSS; Roberts and Lean 2008), a neighborhood spatial verification statistic, was used as one of the precipitation verification metrics. We also used the categorical performance diagram (Roebber, 2009), which combines key information of the frequency bias (FR), probability of detection (POD), critical success index (CSI) and success ratio [SR, one minus the false alarm rate (FAR)], into one diagram to evaluate the impact of the lightning DA scheme relative to the impact of other experiments.

Figs. 7a-b show a comparison of the FSS with two different rainfall thresholds

for the first three forecast hours initialized at 2000 on 13 July 2017. Benefitting from the convective-scale DA, experiments RA, LN and RALN have higher scores than CTL for both the 2.5 mm (moderate precipitation) and the 15 mm (heavy precipitation) thresholds, and RALN further improves the precipitation skill compared with the experiments assimilating either data type alone. Figs. 7c-d show the categorical performance diagrams for the same two hourly precipitation thresholds. A perfect forecast will be placed toward the upper-right portion of the diagram, indicating a high POD and SR (and hence a high SCI) and near-unity bias. The improvement of the convective-scale DA over CTL is evident, as shown by the higher POD and CSI from RA and RALN. During the 3-h forecast, RALN produces the best overall performance as measured by the higher SR and POD as well as smaller bias (closer to the value of 1). It is also noted that the benefit of lightning DA is greater for the higher precipitation threshold, which is not surprising because of the connection of lightning flashes to strong storm updrafts. The above statistics show that the lightning DA scheme works well in producing updrafts at lightning locations and hence improves the convective rainfall formation. When the lightning DA scheme is combined with radar DA, although the initial moisture fields are the same in experiments RA and RALN due to the assimilation of radar reflectivity observations, in RALN, the enhanced low-level dynamical lifting leads to the accelerated formation of precipitation.

Fig. 7

By comparing the hourly accumulated precipitation distributions against the radar QPE products, we found that the areal coverages of the 1st hour precipitation forecasts in experiments RA, LN and RALN are much improved over that in CTL in the northeastern section of the squall line (2000-2100, Figs. 8a-e). Nevertheless, in the southwestern section of the squall line, the pseudo-convergence observations improve the convective rainfall forecast, and the RALN precipitation forecast is in better

agreement with the QPE, a clear positive impact resulting from the additional lightning DA. For the 2nd hour precipitation forecasts (2100-2200, Figs. 8f-j), the forecasted rainfall in CTL is much weaker than the QPE, and LN outperforms CTL and forecasts several scattered rainfall centers. While both RA and RALN successfully forecast the rain band at the second forecast hour, the precipitation system from RALN is more organized and located slightly to the south of that from RA (closer to the 400-m elevation contour, especially for the southwestern section), which is in better agreement with the observed rain band location. It should be noted that the lightning-alone experiment LN might perform better if a moisture adjustment scheme had been implemented (e.g., Fierro et al. 2019; Chen et al. 2019; Hu et al. 2020). The moisture adjustment was not applied in the current study because our focus here is on the role of kinematic pseudo-observation and the optimal combination of humidity pseudo-observations derived from radar reflectivity and lightning data deserves a more detailed and separate study, which is being explored and will be reported in a follow-up paper.

Fig. 8

b. Impact of lightning DA on analysis fields

To fully elaborate the roles of different data sources in the ability of generating balanced initial fields, we analyzed the dynamical and microphysical characteristics. Though LN shows improved convective precipitation forecast compared with CTL, such positive impact is less significant due to the less updated microphysics, and hence we focused on the differences between experiment RA and RALN. Fig. 9 shows the analysis wind and convergence fields as well as the increments in the water vapor at different vertical levels. Comparing RA and RALN with CTL, we found that water vapor increments greater than 2 g kg^{-1} are obtained at 700 hPa from the assimilation of reflectivity data. The assimilation of radial wind observations in RA (Figs. 9c-d) enhances the northwesterly flows behind the squall line in comparison

559 with CTL, and the convergence, especially behind the northeastern section of the
560 squall line, is also strengthened. The contribution of lightning DA to the wind analysis
561 is reflected by the enhanced northwesterly winds and horizontal wind convergence in
562 RALN behind the southwestern section of the squall line at both 700 hPa and 500 hPa
563 compared to RA (Figs. 9e-f).

564 **Fig. 9**

565

566 The impact of lightning DA on the wind analysis can be clearly visualized by
567 plotting the wind difference and convergence difference between RALN and CTL and
568 between RALN and RA (Fig. 10). The combined assimilation of these two data
569 sources generates a wide convergence band along the squall line (Fig. 10a). The main
570 area with strengthened wind convergence in RALN compared with that in RA is
571 located in the southwestern section behind the squall line (Fig. 10b), where none of
572 the radars have good observation coverage.

573 **Fig. 10**

574

575 The vertical velocity, layer-averaged water vapor mixing ratio between 700 hPa
576 and 500 hPa, and convective available potential energy (CAPE) fields at 2006 on 13
577 July 2017 (6-min model integration after DA) are compared in Fig. 11 among the
578 three experiments. The 6-min model integration was chosen because these fields were
579 spun up after the short model integration in response to the updated horizontal wind
580 analysis. The northwesterly flows at 850 hPa over the mountainous regions in RA (Fig.
581 11b) are increased relative to those in CTL (Fig. 11a) due to the radial wind DA,
582 leading to enhanced convergence and upward vertical motions. When both radar and
583 lightning data are assimilated, the magnitudes of the northwesterly and southwesterly
584 winds are further increased, which leads to stronger and wider updrafts in RALN (red
585 arrow in Fig. 11c). Although the moisture fields at the analysis time are the same
586 between RA and RALN from the contribution of the reflectivity assimilation, the

enhanced updrafts in RALN transport more low-level water vapor upward and accelerate the formation of precipitation (Fig. 11f). Additionally, because of the adjusted vertical distribution of moisture, the CAPE over the western mountainous areas is increased in RALN (Fig. 11i). In short, the above analysis indicates that assimilating total lightning data through the direct update of kinematic states accelerates the formation of updrafts, which causes the redistribution of moisture and hence increases atmospheric instability and hydrometeor production. The results are similar to the studies of Fierro at al. (2015, 2016) based on moisture adjustment in which the buoyancy-generated lifting through the assimilation of moisture pseudo-observation was also induced but at the cost of increased wet biases in short-term forecast. The current lightning DA scheme does not directly employ a moisture assimilation scheme and the updated moisture fields are solely based on reflectivity DA.

Fig. 11

The impact of assimilating the two different types of observations on reducing analysis errors was quantitatively evaluated. Fig. 12 shows the root-mean-square errors (RMSE) of the radial velocity analysis verified against the Beijing Doppler radar data and of the horizontal wind components, temperature, and water vapor analyses against the surface METAR observations. Although radial velocity observations are not an independent dataset for the purpose of a strict verification, an RMSE evaluation can provide a check of whether the assimilation of additional lightning information is done properly such that it helps improve the fitting to the radial velocity. As shown in Fig. 12a, the RMSE of the radial wind field is significantly reduced in RALN compared with that in RA, while both RMSEs are much smaller than that in CTL. The RMSE of the surface u and v winds computed against the surface measurements are also improved (Fig. 12b). Because assimilating the CON pseudo-observations updates only the horizontal winds, the surface moisture

and temperature fields in RALN are not changed relative to those in RA. The improved wind analysis results in low-level convergence (and hence updraft) that enhances the moisture in the western mountainous region shortly after the WRF forecast commences. The above comparisons suggest that assimilating total lightning data in addition to radar data provides additional kinematic information that helps produce improved initial conditions for the horizontal velocities. In the following analysis, the impact of lightning DA on different updated kinematic states and storm evolution forecasts will be illustrated.

Fig. 12

c. Sensitivity of lightning DA to the prescribed *w* profile

The lightning-derived *w* observations for DA depend on the model-based *w* profile and the w_{max} inferred from total lightning flash observations. As shown in Fig. 4a, the *w* profiles obtained with different convective metrics differ in regard to the height of the strongest updraft and the low-level *w* magnitude and hence provide different values of pseudo-*w* observations. To evaluate how sensitive the lightning DA scheme is to the prescribed *w* profile, five assimilation and forecast experiments, each using one of the five *w* profiles in Fig. 4a, were conducted. Fig. 13 shows the averaged vertical velocity and rainwater mixing ratio profiles during the 1st forecast hour in each sensitivity experiment. Compared with the baseline RA experiment, we found that generally, the *w* profiles based on the updraft intensity as the metric of deep convection (e.g., UP10, UP15) produce stronger upward vertical motions and higher rainwater production. The *w* profiles based on the volume maximum graupel mixing ratio (QG5 and QG7) generate weaker updrafts, especially at low levels, and lower rainwater mixing ratios. In terms of the precipitation forecast performance (Fig. 14), the experiments using updraft-based *w* profiles produce slightly higher scores than those obtained in RA, while the graupel-based *w* profiles produce lower scores. It is not surprising that the mean profile (AVE) produces an improved precipitation

forecast, as shown by the highest FSS, because this profile accounts for both dynamical and microphysical contributions.

Fig. 13

Comparing the vertical distributions of the CON pseudo-observations estimated from these *w* profiles (Fig. 4b), the main difference is that the UP10 and UP15 profiles give larger values of convergence at low levels, which can produce larger low-level dynamical lifting that forces air parcels to reach the condensation level, resulting in enhanced rainwater production. Compared with UP10 and UP15, the graupel-based *w* profiles (QG5 and QG7) have larger convergence values within the mixed-phase region above the freezing level that support the maintenance of large ice-phase particles but smaller values of convergence at low levels; these conditions may not enable the air parcels to be lifted high enough to overcome the convective inhibition and reach their LFC to form clouds. As a result, the averaged updraft intensity and rainfall production in QG5 and QG7 are much weaker than those in UP10 and UP15. The mean *w* profile, AVE, with moderate low-level and mid-level convergence, is capable of producing stronger and deeper updrafts as well as higher rainwater mixing ratios, which contributes to the best FSS for both light and heavy precipitation, as shown in Fig. 14.

Fig. 14

d. Heavy rainfall case on 16 July 2018

The analyses presented in the previous sections demonstrate the improved convective analysis fields and forecasts from the new lightning DA scheme. To verify the robustness of the scheme, another convective case over Beijing is examined using the same DA and model configurations without changing any of the input parameters. Influenced by an upper-level shortwave trough and a strong low-level southwest jet, several convective cells developed along a convergence line over Beijing at 0000 on

16 July 2018 and gradually merged and grew upscale into a mesoscale convective system (MCS). The MCS propagated into central Beijing at 0400 and produced frequent lightning flashes, as shown in Fig. 15. More than half of the ground-based automatic weather stations distributed over Beijing reported more than 100 mm of rainfall during the lifespan of the MCS, and several stations even recorded rainfall over 200 mm.

Fig. 15

Fig. 16 shows the 1-h forecast of the composite radar reflectivity fields initialized at 0400. Although CTL is able to produce some of the observed storms, the convective storm is very limited in regard to its areal coverage (Fig. 16b). The assimilation of radar data improves the forecast of the southern portion of the MCS; however, the convection over northeastern Beijing is very weak (black arrow in Fig. 16c). With another 1 h of integration, only a single convective cell forms in northeastern Beijing (not shown). The additional assimilation of LMI lightning data enhances the low-level convergence and increases the convection intensity on the northeastern border of Beijing (Fig. 16d), producing a rainfall area with higher than 30 dBZ reflectivity similar to the observations. Consistent with the squall line case analyzed above, RALN outperforms RA and CTL in terms of the FSS of the composite radar reflectivity and produces higher POD and CSI for different thresholds (Fig. 17).

Fig. 16

Fig. 17

Fig. 18 shows a comparison of the 3-h accumulated precipitation among the CTL, RA, and RALN experiments initialized at 0400 on 16 July 2018. The observed rainfall structure consists mainly of two precipitation areas located near the northeastern (black arrow in Fig. 18a) border of Beijing and to the east (red arrow) of

Beijing. A thin rainband is forecasted to the east of Beijing in CTL, but the overall precipitation coverage is significantly smaller than the observations, and the rainfall area near the northeastern border of Beijing is largely missed (Fig. 18b). The assimilation of reflectivity and radial wind observations in RA broadens the precipitation coverage by more than 3.2 mm compared with CTL, and the heavier rainfall to the east of Beijing shows a two-band structure (red arrow in Fig. 18c), similar to the observed structure. Comparing RALN with RA, we found that the two-band rainfall to the east of Beijing is well captured in both experiments; however, a clear difference occurs near the northeastern border of Beijing, where heavier rainfall is forecasted in RALN (Fig. 18d), which agrees well with the observations.

Fig. 18

The verification statistics shown in Fig. 19 are consistent with those for the 13 July 2017 squall case. The extra kinematic information from lightning data produces better FSS and higher POD and SR in RALN than in RA and CTL. Overall, the assimilation of LMI lightning data in conjunction with radar data shows positive impact on the short-term forecasts of convective precipitation. Similar to the squall line case, the enhanced low-level convergence via lightning DA directly forms updrafts at lightning observation locations (not shown here), which accelerates the precipitation process and results in improved precipitation forecasts.

Fig. 19

6. Summary and conclusions

The strong connection between the total lightning flash rate and storm updraft has been confirmed both by field observations and by numerical studies. In this study, we showed that such a relationship could be used in the assimilation of space-borne lightning data to provide important convective-scale kinematic information for model initialization. We presented a lightning data assimilation scheme that was developed

724 in the WRFDA 3DVar system to update model kinematic states. This scheme
725 combines total lightning observations and model-based prescribed vertical velocity
726 conditions to retrieve useful kinematic information for convective-scale DA.
727 Specifically, the magnitudes of column-maximum updrafts (w_{max}) are derived from
728 the total lightning observations mainly following the idea of the PR92 lightning
729 parameterization scheme. A prescribed profile from model forecast data providing the
730 vertical distribution of the vertical velocity w enables the w_{max} information to spread
731 out over the whole grid column to create pseudo-w observations. Since WRFDA
732 3DVar utilizes the horizontal wind components u and v as its momentum control
733 variables, the derived w fields are converted into pseudo-horizontal convergence
734 observations based on the mass continuity equation. An observation term
735 corresponding to the lightning-derived convergence is incorporated into the total cost
736 function of 3DVar.

737 Considering the proven role of radar observations in convective-scale data
738 assimilation, we evaluated the impact of the assimilation of lightning data in addition
739 to radar data, in order to examine whether assimilating the derived kinematic
740 information from the total lightning observations adds any value to the current radar
741 DA in 3DVar. A series of single observation tests were conducted first to illustrate the
742 impact of assimilating two different types of kinematic observations, namely, the
743 radar radial velocity and pseudo-lightning-derived convergence. The results showed
744 that the combined assimilation of radar radial velocity and lightning-derived
745 pseudo-convergence observations could effectively enhance low- and mid-level wind
746 convergence and reduce the errors between the observations and model background
747 compared to assimilating either data type alone.

748 After confirming the feasibility of the lightning DA scheme to update model
749 kinematic states with single observation tests, real case studies were performed. A
750 squall line event that occurred over Beijing in 2017 was used to illustrate the positive
751 impact of assimilating space-borne LMI observations in addition to radar observations

on improving model analysis and storm forecasting. Three experiments, namely, assimilating neither radar nor lightning data (CTL), assimilating radar data only (RA), and assimilating both radar and lightning data (RALN), were conducted. The results showed that the new lightning DA scheme in conjunction with the assimilation of radar data produced improved precipitation forecasts compared to the radar DA only experiment. We further showed that the extra kinematic information from lighting data could effectively reduce model wind errors and enhance low-level convergence. Provided thermodynamic and microphysical fields identical to those in RA through the assimilation of reflectivity data, the assimilation of lightning-derived convergence observations in RALN enhanced the updrafts at lightning observation locations, which could in turn increase the upward transport of low-level moisture and accelerate rainwater production. Our quantitative verification of the performance of short-term convective forecasts showed that the lightning DA added value to the radar DA by improving the precipitation forecast skill over the assimilation of radar data alone experiment. The new lightning DA scheme was further applied to a heavy rainfall case in 2018, and the results confirmed the effective and robust improvement in storm forecasting.

Our study demonstrated that lightning observations such as those from space-borne lightning imagers can complement current radar observational networks, allowing us to better resolve the nature of clouds when used together. The combined assimilation scheme can be further improved in the future. Using data from different sources together can also potentially help improve quality control and the quantification of observation errors. For example, one issue that deserves future research is to develop a method to account for signal attenuation in space-borne lightning detection by optically deep clouds, which is not considered in the current study. One possible approach is to determine whether signal attenuation occurs using the vertical distribution of radar reflectivity. With an aim to provide more balanced initial fields, the combined assimilation of radar and lightning data can also be

improved by employing lightning information in the radar reflectivity-based humidity or latent heat adjustment scheme. For example, the moisture insertion with reference to electrical states of thunderstorms is plausible to acquire small-scale water vapor variations (Fierro et al. 2019; Hu et al. 2020). A “drying” procedure could be developed to balance the moisture adjustment and reduce spurious convection by cooperating radar data (Gao et al. 2018) and lightning observations. Furthermore, the performance of the combined assimilation of radar and lightning data can be further studied with more advanced 4DVar assimilation techniques that employ dynamical model constraints (Wang et al. 2013b).

Acknowledgments

The work was supported by the National Natural Science Foundation of China (grant 41630425 and 41761144074) and the Key Research Program of Frontier Sciences, CAS (QYZDJ-SSW-DQC007). The author Zhixiong Chen is supported by the Chinese Scholarship Council (CSC) and thanks NCAR for hosting his visit. The computing resources used in this study were provided by NCAR CISL. This work complies with the AGU data policy. The WRF and WRFDA model (Version 3.9.1) and their documentation are available for download through the WRF website (https://www.mmm.ucar.edu/weather-research-and-forecasting-model) supported by the Mesoscale and Microscale Meteorology Laboratory (MMM) of NCAR. Other important data supporting the conclusion of the paper are available in the main text. Refer to the data repository website (https://zenodo.org/record/3901539) or contact the author (chenzx@mail.iap.ac.cn) for more detailed data.

804 **References**

805 Alexander, G. D., J. A. Weinman, V. Karyampudi, W. S. Olson, and A. C. L. Lee,
806 1999: The effect of assimilating rain rates derived from satellites and lightning
807 on forecasts of the 1993 Superstorm. Mon. Wea. Rev., 127, 1433–1457.

808 Barker, D. M., W. Huang, Y.-R. Guo, A. J. Bourgeois, and Q. N. Xiao, 2004: A
809 three-dimensional variational data assimilation system for MM5: Implementation
810 and initial results. Mon. Wea. Rev., 132, 897–914.

811 Bougeault, P. and P. Lacarrere, 1989: Parameterization of orography-induced
812 turbulence in a mesobeta-scale model. Mon. Wea. Rev., 117, 1872-1890.

813 Calhoun, K. M., D. R. MacGorman, C. L. Ziegler, and M. I. Biggerstaff, 2013:
814 Evolution of lightning activity and storm charge relative to dual-Doppler analysis
815 of a high- precipitation supercell storm. Mon. Wea. Rev., 141, 2199– 2223.

816 Cao, D., F. Lu, X. Zhang, Z. Zhang, Q. Liu, 2018: Lightning rate and its relationship
817 with intensity of typhoons over the Northwest Pacific. XVI International
818 Conference on Atmospheric Electricity, 17–22 June 2018, Nara city, Nara, Japan.

819 Chen, M., Y. Wang, F. Gao, and X. Xiao, 2012: Diurnal variations in convective
820 storm activity over contiguous North China during the warm-season based on
821 radar mosaic climatology, J. Geophys. Res., 117, D20115.

822 Chen, M., Y. Wang, F. Gao, and X. Xiao, 2014: Diurnal evolution and distribution of
823 warm‐season convective storms in different prevailing wind regimes over
824 contiguous North China, J. Geophys. Res., 119, 2742-2763.

825 Chen Z, X, Qie, D, Liu, Y, Xiong, 2019. Lightning data assimilation with
826 comprehensively nudging water contents at cloud-resolving scale using WRF
827 model. Atmos. Res., 22: 72–87.

828 Chen, F., and J. Dudhia, 2001: Coupling an advanced land surface-hydrology model
829 with the Penn State-NCAR MM5 modeling system. Part I: Model
830 implementation and sensitivity. Mon. Wea. Rev., 129, 569–585.

831 Christian, H. J., and Coauthors, 1999: The Lightning Imaging Sensor. Proc. 11th Int.

Conf. on Atmospheric Electricity, Guntersville, AL, International Commission on Atmospheric Electricity, 746–749.

Deierling, W., and Petersen, W. A., 2008: Total lightning activity as an indicator of updraft characteristics, J. Geophys. Res., 113, D16210.

Deshpande, S.M., N, Dhangar, S. K. Das, M. C. R. Kalapureddy, K, Chakravarty, S, Sonbawne, and M, Konwar, 2015: Mesoscale kinematics derived from X-band Doppler radar observations of convective versus stratiform precipitation and comparison with GPS radiosonde profiles. J. Geophys. Res., 120, 11,536–11,551.

Dudhia, J., 1989: Numerical study of convection observed during the winter monsoon experiment using a mesoscale two-dimensional model. J. Atmos. Sci., 46, 3077–3107.

Fierro, A. O., E. R. Mansell, C. L. Ziegler, and D. R. MacGorman, 2012: Application of a lightning data assimilation technique in the WRF-ARW model at cloud-resolving scales for the tornado outbreak of 24 May 2011. Mon. Wea. Rev., 140, 2609– 2627.

Fierro, A. O., J. Gao, C. L. Ziegler, E. R. Mansell, D. R. MacGorman, and S. R. Dembek, 2014: Evaluation of a cloud-scale lightning data assimilation technique and a 3DVAR method for the analysis and short-term forecast of the 29 June 2012 derecho event. Mon. Wea. Rev., 142, 183–202.

Fierro, A. O., A. Clark, E. R. Mansell, D. R. MacGorman, S. R. Dembek, and C. L. Ziegler, 2015: Impact of storm-scale lightning data assimila- tion on WRF-ARW precipitation forecasts during the 2013 warm season over the contiguous United States. Mon. Wea. Rev., 143, 757–777.

Fierro, A. O., J. Gao, C. L. Ziegler, K. M. Calhoun, E. R. Mansell, and D.R. MacGorman, 2016: Assimilation of flash extent data in the variational framework at convection-allowing scales: Proofof-concept and evaluation for the short-term forecast of the 24 May 2011 tornado outbreak. Mon. Wea. Rev., 144,

4373– 4393.

Fierro, A. O., Y. Wang, J. Gao, and E. R. Mansell, 2019: Variational assimilation of radar data and GLM lightning-derived water vapor for the short-term forecasts of high-impact convective events. Mon. Wea. Rev., 147, 4045–4069.

Gao, S., J. Sun, J. Min, Y. Zhang, and Z. Ying, 2018: A scheme to assimilate ‘‘no rain’’ observations from Doppler radar. Wea. Forecasting, 33, 71–88.

Goodman, S. J., and Coauthors, 2013: The GOES-R Geostationary Lightning Mapper (GLM). Atmos. Res., 125–126, 34–49.

Gustafsson, N., and Coauthors, 2018: Survey of data assimilation methods for convective-scale numerical weather prediction at operational centres. Quart. J. Roy. Meteor. Soc., 144, 1218– 1256.

Houze, R. A., Jr., 1982: Cloud clusters and large-scale vertical motions in the tropics. J. Meteorol. Soc. Jpn, 60, 396–410.

Hu, J., A. O. Fierro, Y. Wang, J. Gao, and E. R. Mansell, 2020: Exploring the assimilation of GLM derived water vapor mass in a cycled 3DVAR framework for the short-term forecasts of high impact convective events. Mon. Wea. Rev., 148, 1005–1028.

Hui W., F. Huang and R. Liu, 2020: Characteristics of lightning signals over the Tibetan Plateau and the capability of FY-4A LMI lightning detection in the Plateau, International Journal of Remote Sensing, 41:12, 4603-4623.

Janjic, T., and Coauthors, 2017: On the representation error in data assimilation. Quart. J. Roy. Meteor. Soc., 144, 1257–1278

Kain J S, and J. M. Fritsch. 1998: Multiscale convective overturning in mesoscale convective systems: reconciling observations, simulations, and theory. Mon. Wea. Rev., 126, 2254-2273.

Kong, R., M. Xue, A. O. Fierro, Y. Jung, C. Liu, E. R. Mansell, and D. R. MacGorman, 2020: Assimilation of GOES-R Geostationary Lightning Mapper flash extent density data in GSI EnKF for the analysis and short-term forecast of

a Mesoscale Convective System. Mon. Wea. Rev., 148, 2111–2133.

Kuhlman, K. M., C. L. Ziegler, E. R. Mansell, D. R. MacGorman, and J. M. Straka, 2006: Numerically simulated electrification and lightning of the 29 June 2000 STEPS supercell storm. Mon. Wea. Rev., 134, 2734-2757.

MacGorman, D. R., D. W. Burgess, V. Mazur, W. D. Rust, W. L. Taylor, and B. C. Johnson, 1989: Lightning rates relative to tornadic storm evolution on 22 May 1981. J. Atmos. Sci., 46, 221–251.

Mach, D. M., H. J. Christian, R. J. Blakeslee, D. J. Boccipio, S. J. Goodman, and W. L. Boeck, 2007: Performance assessment of the Optical Transient Detector and Lightning Imaging Sensor. J. Geophys. Res., 112, D09210.

Mansell, E. R., C. L. Ziegler, and D. R. MacGorman, 2007: A lightning data assimilation technique for mesoscale forecast models. Mon. Wea. Rev., 135, 1732–1748.

Mansell, E. R., C. L. Ziegler, and E. C. Bruning, 2010: Simulated electrification of a small thunderstorm with two-moment bulk microphysics. J. Atmos. Sci., 67, 171–194.

Mansell, E. R., 2014: Storm-scale ensemble Kalman filter assimilation of total lightning flash data. Mon. Wea. Rev., 142, 3683– 3695.

Mapes, B. E., and R. A. Houze Jr., 1995: Diabatic divergence profiles in western Pacific mesoscale convective systems. J. Atmos. Sci., 52, 1807–1828.

Mapes, B.E. and J. Lin, 2005: Doppler radar observations of mesoscale wind divergence in regions of tropical convection. Mon. Wea. Rev., 133, 1808− 1824.

Mlawer, E. J., S. J. Taubman, P. D. Brown, M. J. Iacono, and S. A. Clough, 1997: Radiative transfer for inhomogeneous atmosphere: RRTM, a validated correlated-k model for the longwave. J. Geophys. Res., 102, 16663–16682.

Papadopoulos, A., T. G. Chronis, and E. N. Anagnostou, 2005: Improving convective precipitation forecasting through assimilation of regional lightning measurements in a mesoscale model. Mon. Wea. Rev., 133, 1961–1977.

916 Parrish, D. F., and J. C. Derber, 1992: The National Meteorological Center's spectral
917 statistical-interpolation analysis system. Mon. Wea. Rev., 120, 1747–1763.
918 Pessi, A. T., and S. Businger, 2009: The impact of lightning data assimilation on a
919 winter storm simulation over the North Pacific Ocean. Mon. Wea. Rev., 137,
920 3177–3195.
921 Peterson, M., 2019: Research applications for the Geostationary Lightning Mapper
922 operational lightning flash data product. J. Geophys. Res. Atmos., 124,
923 10205–10231.
924 Price, C., and D. Rind, 1992: A simple lightning parameterization for calculating
925 global lightning distributions. J. Geophys. Res., 97, 9919–9933.
926 Qie, X.; R, Zhu, T, Yuan, X, Wu, W Li, D Liu, 2014: Application of total-lightning
927 data assimilation in a mesoscale convective system based on the WRF model.
928 Atmos. Res., 145, 255–266.
929 Roberts, N. M., and H. W. Lean, 2008: Scale-selective verification of rainfall
930 accumulations from high-resolution forecasts of convective events. Mon. Wea.
931 Rev., 136, 78–97.
932 Roebber, P. J., 2009: Visualizing multiple measures of forecast quality. Wea.
933 Forecasting, 24, 601–608.
934 Schultz, C. J., W. A. Petersen, and L. D. Carey, 2011: Lightning and severe weather:
935 A comparison between total and cloud- to-ground lightning trends. Wea.
936 Forecasting, 26, 744–755.
937 Sun, J., 2005: Initialization and numerical forecasting of a supercell storm observed
938 during STEPS. Mon. Wea. Rev., 133, 793–813.
939 Sun, J., and Coauthors, 2014: Use of NWP for nowcasting convective precipitation:
940 Recent progress and challenges. Bull. Amer. Meteor. Soc., 95, 409–426.
941 Sun, J., H. Wang, W. Tong, Y. Zhang, C.-Y. Lin, and D. Xu, 2016: Comparison of the
942 impacts of momentum control variables on high-resolution variational data
943 assimilation and precipitation forecasting. Mon. Wea. Rev., 144, 149–169.

Tong, W., G. Li, J. Sun, X. Tang, and Y. Zhang, 2016: Design strategies of an hourly update 3DVAR data assimilation system for improved convective forecasting. Wea. Forecasting, 31, 1673–1695.

Wang, H., and Coauthors, 2017: Improving lightning and precipitation prediction of severe convection using lightning data assimilation with NCAR WRF-RTFDDA. J. Geophys. Res. Atmos.,122,12296–12316.

Wang, H., J. Sun, S. Fan, and X.-Y. Huang, 2013a: Indirect assimilation of radar reflectivity with WRF 3D-Var and its impact on prediction of four summertime convective events. J. Appl. Meteor. Climatol., 52, 889–902.

Wang, H., J. Sun, X. Zhang, X. Huang, and T. Auligné, 2013b: Radar Data Assimilation with WRF 4D-Var. Part I: System Development and Preliminary Testing. Mon. Wea. Rev., 141, 2224–2244.

Xiao, Q., and J. Sun, 2007: Multiple-radar data assimilation and short-range quantitative precipitation forecasting of a squall line observed during IHOP_2002. Mon. Wea. Rev., 135, 3381– 3404.

Yuter, S. E. and R. A. Houze, 1995: Three-dimensional kinematic and microphysical evolution of Florida cumulonimbus. Part II: Frequency distributions of vertical velocity, reflectivity, and differential reflectivity. Mon. Wea. Rev., 123, 1921-1940.

Zhang, R., Y. Zhang, L. Xu, D. Zheng, and W. Yao, 2017: Assimilation of total lightning data using the three-dimensional variational method at convection-allowing resolution. J. Meteor. Res., 31, 731–746.

Zipser, E. J., and K. R. Lutz, 1994: The vertical profile of radar reflectivity of convective cells: A strong indicator of storm intensity and lightning probability? Mon. Wea. Rev., 122, 1751–1759.

Figure Captions：

Fig. 1 Topography of northern China (color, unit: km) and locations (blue crosses) of the six radar stations distributed around Beijing with their coverage (orange circles)

Fig. 2 Schematic diagram of the calculation of the LMI event density (LED) in the WRF model Cartesian grid. The pixel resolution of the LMI event product is 7.8 km, the search radius R is set to 5 km, and the number of 15-min binned LMI lightning events at each model grid is counted as the LED. For example, suppose the horizontal grid spacing (dx) is 2 km here; the LED for the green, orange, red and blue grids are 4, 6, 3 and 1, respectively

Fig. 2 Schematic diagram of the calculation of the LMI event density (LED) in the WRF model Cartesian grid. The pixel resolution of the LMI event product is 7.8 km, the search radius R is set to 5 km, and the number of 15-min binned LMI lightning events at each model grid is counted as the LED. For example, suppose the horizontal grid spacing (dx) is 2 km here; the LED for the green, orange, red and blue grids are 4, 6, 3 and 1, respectively

Fig. 3 Cumulative distribution function of the 15-min binned LMI event density

Fig. 4 (a) Profiles of the normalized vertical velocity *w* under different convective scenarios and (b) convergence profiles corresponding to the *w* profiles calculated via the mass continuity equation. UP 10 and UP15 represent the profiles with maximum updraft intensities (up_{max}) over 10 m s^{-1} and 15 m s^{-1}, respectively, QG5 and QG7 represent the profiles with maximum graupel mixing ratios (qg_{max}) over 5 g kg^{-1} and 7 g kg^{-1}, respectively, and AVE represents the averaged profile using all the vertical velocity *w* fields of the four convective scenarios. (c) Vertical distributions of the standard deviation and mean of the CON pseudo-observations

998

999 Fig. 5 Analysis increments in the wind field (vector: m s^{-1}, and the magnitude of
1000 reference wind is 0.3 m s^{-1}) and horizontal wind convergence field (color: 10^{-3} s^{-1}) for
1001 the single observation tests at 700 hPa: (a) RA, (b) LN and (c) RALN

1002

1003 Fig. 6 (a) Composite radar reflectivity (unit: dBZ) at 2000 on 13 July 2017 and
1004 (b) LMI lightning event density (unit: 15 min^{-1}) from the LMI between 1945 and 2000.
1005 The brown contour lines denote the 25-dBZ and 45-dBZ contour lines. The dashed
1006 purple line denotes the 400-m terrain elevation

1007

1008 Fig. 7 (a-b) FSS of the hourly accumulated precipitation and (c-d) performance
1009 diagrams for each of the first three forecast hours with thresholds of 2.5 mm (left
1010 column) and 15 mm (right column) for the CTL (yellow), RA (green), LN (blue) and
1011 RALN (red) experiments initialized at 2000 on 13 July 2017. The results are shown
1012 for a neighborhood radius of 10 km. In the performance diagrams, the horizontal axis
1013 represents the success ratio (SR), the vertical axis represents the probability of
1014 detection (POD), the magenta lines represent the critical success index (CSI), the
1015 black dashed lines represent the frequency bias (FR), and the numbers inside the solid
1016 circles represent the forecast hour

1017

1018 Fig. 8 Hourly accumulative precipitation (color, unit: mm) during the (a-e) 1st
1019 and (f-j) 2nd forecasting hour initialized at 2000 on 13 July 2017 for the radar QPE
1020 observations (1st column) and for the CTL (2nd column), RA (3rd column), LN (4th
1021 column) and RALN (5th column) experiments. The dashed purple line denotes the
1022 400-m terrain elevation

1023

1024 Fig. 9 Wind fields (vectors, the magnitude of the reference wind is 12 m s^{-1}) and
1025 wind convergence fields (color: 10^{-3} s^{-1}) for the (a-b) CTL, (c-d) RA and (e-f) RALN

experiments at 700 hPa (left) and 500 hPa (right) at 2000 on 13 July 2017. The solid magenta contour lines (starting at 2 g kg^{-1} with an interval of 2 g kg^{-1}) denote the increments in the water vapor mixing ratios in RA and RALN. The long dashed red line denotes the location of the observed squall line, and the short purple line denotes the 400-m terrain elevation

Fig. 10 Wind vector difference (vectors, the magnitude of the reference wind is 12 m s^{-1}) and convergence difference (color: 10^{-3} s^{-1}) between (a) RALN and CTL and (b) between RALN and RA at 700 hPa at 2000 on 13 July 2017. The long dashed red line denotes the location of the observed squall line, and the short purple line denotes the 400-m terrain elevation

Fig. 11 (a-c) Vertical velocity *w* (color, unit: m s^{-1}) at 700 hPa superimposed by the 850-hPa horizontal wind field (vectors, the magnitude of the reference wind is 10 m s^{-1}), (d-f) layer-averaged water vapor mixing ratio (color, unit: g kg^{-1}) and rainwater mixing ratio (contour lines with values of 0.1 g kg^{-1}) between 700 hPa and 500 hPa, and (g-i) horizontal distribution of the maximum convective available potential energy (color, unit: J kg^{-1}) for the CTL (left), RA (center) and RALN (right) experiments at 2006 on 13 July 2017

Fig. 12 RMSE of the (a) radial velocity verified against the Beijing Nanyuan Doppler radar observations and of the (b) wind components, temperature and water vapor mixing ratio compared with surface METAR observations

Fig. 13 Averaged vertical velocity profile (a) over the inner domain and (b) over lightning regions and the (c) rainwater mixing ratio profile over lightning regions for the 1^{st} hour forecasts during 2000-2100 on 13 July 2017

Fig. 14 FSS of the 1st hour accumulated precipitation forecasts during 2000-2100 on 13 July 2017 with thresholds of (a) 2.5 and (b) 15 mm for all sensitivity experiments

Fig. 15 (a) Composite radar reflectivity (unit: dBZ) at 0400 on 16 July 2018 and (b) LMI lightning event density (unit: 15 min^{-1}) from the LMI between 0345 and 0400

Fig. 16 Composite radar reflectivity (colors, unit: dBZ) of the (a) radar observations (OBS) and the (b) CTL, (c) RA, and (d) RALN experiments at 0500 on 16 July 2018

Fig. 17 Same as Fig. 7 but for the composite reflectivity fields initialized at 0400 on 16 July 2018 relative to radar observations with thresholds of 30 dBZ (left column) and 40 dBZ (right column)

Fig. 18 Three-hour accumulative precipitation forecasts (color, unit: mm) initialized at 0400 on 16 July 2018 for (a) the radar QPE observations and for the (b) CTL, (c) RA and (d) RALN experiments

Fig. 19 Same as Fig. 7 but for the hourly accumulated precipitation initialized at 0400 on 16 July 2018 relative to radar observations with thresholds of 2.5 mm (left column) and 15 mm (right column)

Table 1. Ranges of the LMI event density and corresponding maximum vertical velocity w_{max}

LMI Event Density (15 min^{-1})	w_{max} (m s^{-1})
2-12	5
13-22	8
23-42	12
43-	15

Table 2. List of single observation tests. In the first row, "CON" stands for the convergence value (unit: 10^{-3} s^{-1}), "RV" stands for the radar radial velocity (unit: m s^{-1}), and the superscripts "obs", "omb" and "oma" stand for the single observation value, its corresponding innovation (observation minus background), and its residual (observation minus analysis), respectively, in each type of single observation

Test	CON^{obs}	CON^{omb}	CON^{oma}	RV^{obs}	RV^{omb}	RV^{oma}
RA	/	/	/	-7.691	-3.147	-0.493
LN	-0.557	-0.702	-0.589	/	/	/
RALN	-0.557	-0.702	-0.584	-7.691	-3.147	-0.489

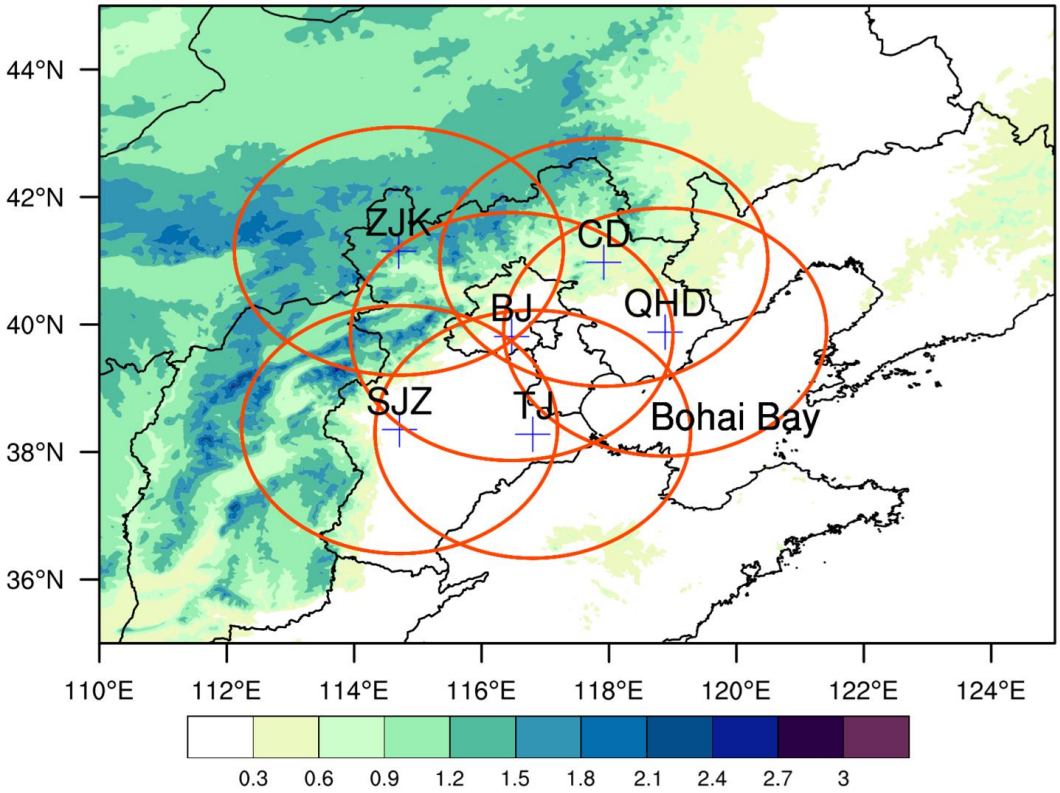

Fig. 1 Topography of northern China (color, unit: km) and locations (blue crosses) of the six radar stations distributed around Beijing with their coverage (orange circles)

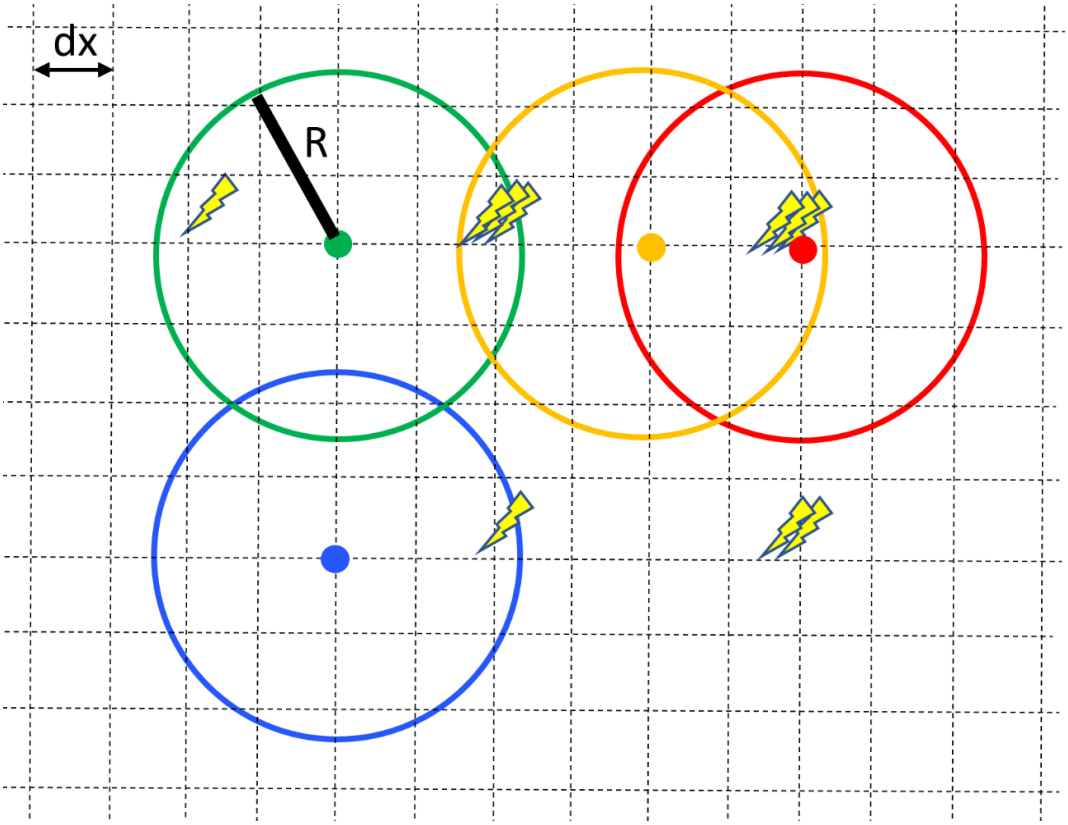

Fig. 2 Schematic diagram of the calculation of the LMI event density (LED) in the WRF model Cartesian grid. The pixel resolution of the LMI event product is 7.8 km, the search radius R is set to 5 km, and the number of 15-min binned LMI lightning events at each model grid is counted as the LED. For example, suppose the horizontal grid spacing (dx) is 2 km here; the LED for the green, orange, red and blue grids are 4, 6, 3 and 1, respectively

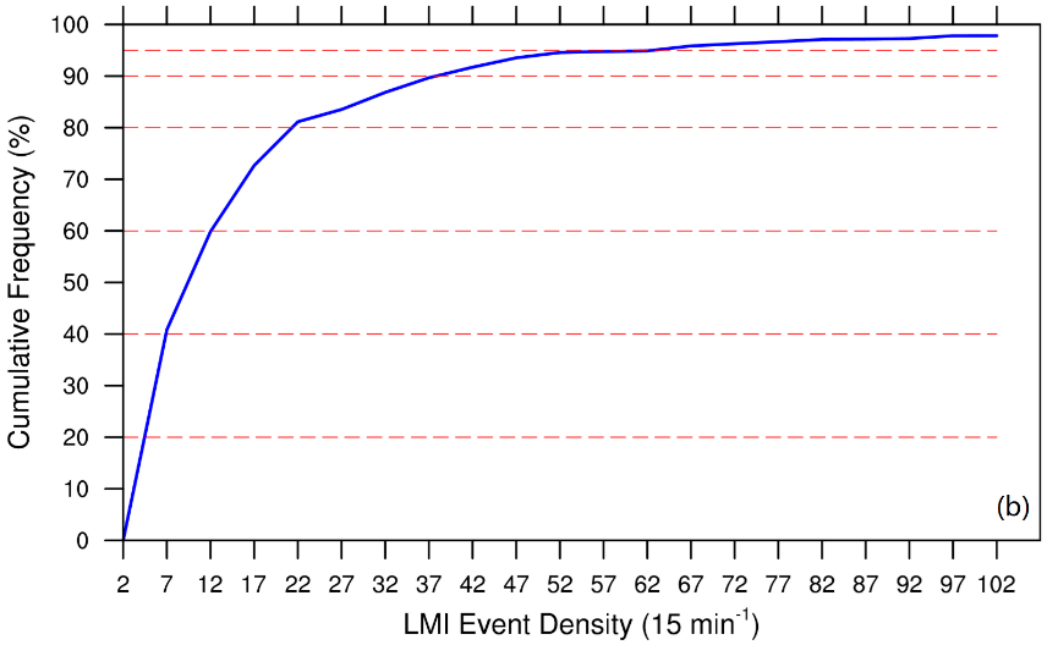

Fig. 3 Cumulative distribution function of the 15-min binned LMI event density

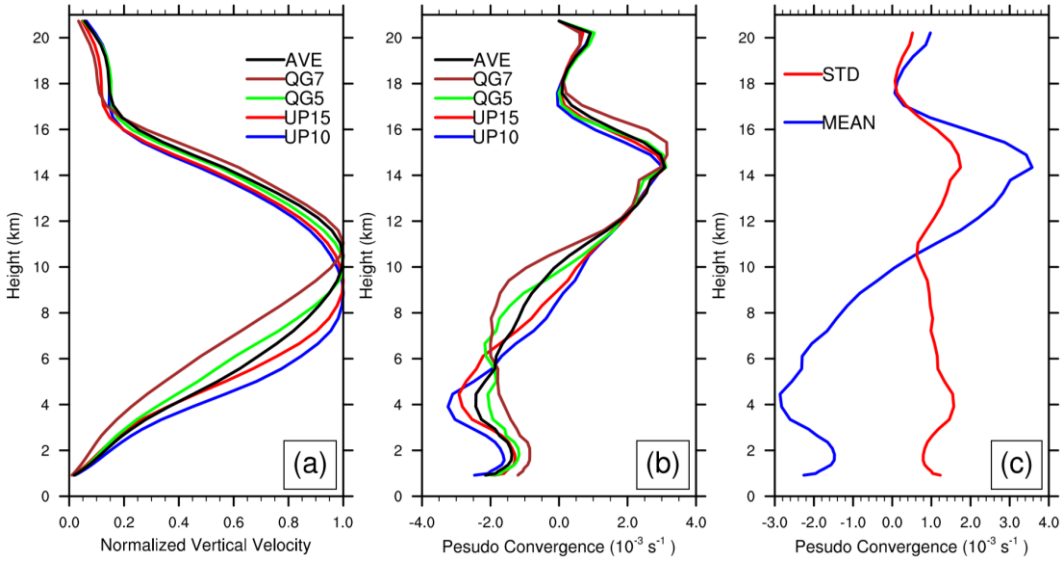

Fig. 4 (a) Profiles of the normalized vertical velocity *w* under different convective scenarios and (b) convergence profiles corresponding to the *w* profiles calculated via the mass continuity equation. UP 10 and UP15 represent the profiles with maximum updraft intensities (up_{max}) over 10 m s^{-1} and 15 m s^{-1}, respectively, QG5 and QG7 represent the profiles with maximum graupel mixing ratios (qg_{max}) over 5 g kg^{-1} and 7 g kg^{-1}, respectively, and AVE represents the averaged profile using all the vertical velocity *w* fields of the four convective scenarios. (c) Vertical distributions of the standard deviation and mean of the CON pseudo-observations

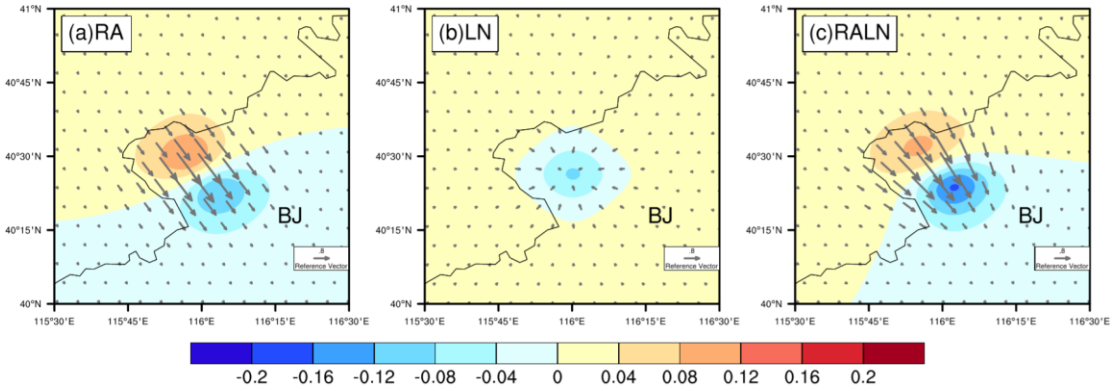

Fig. 5 Analysis increments in the wind field (vector: m s^{-1}, and the magnitude of reference wind is 0.3 m s^{-1}) and horizontal wind convergence field (color: 10^{-3} s^{-1}) for the single observation tests at 700 hPa: (a) RA, (b) LN and (c) RALN

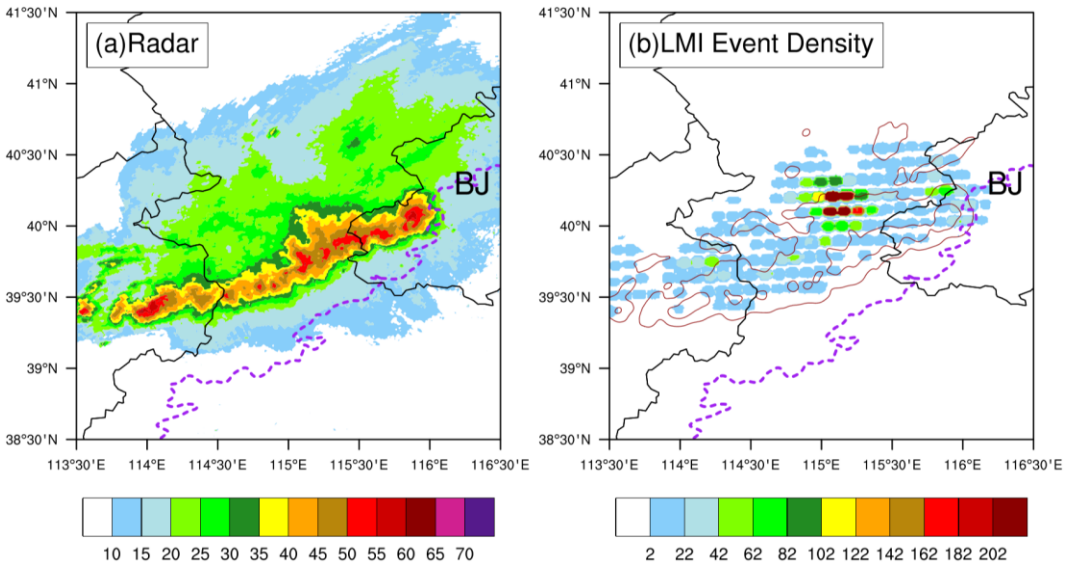

Fig. 6 (a) Composite radar reflectivity (unit: dBZ) at 2000 on 13 July 2017 and (b) LMI lightning event density (unit: 15 min^{-1}) from the LMI between 1945 and 2000. The brown contour lines denote the 25-dBZ and 45-dBZ contour lines. The dashed purple line denotes the 400-m terrain elevation

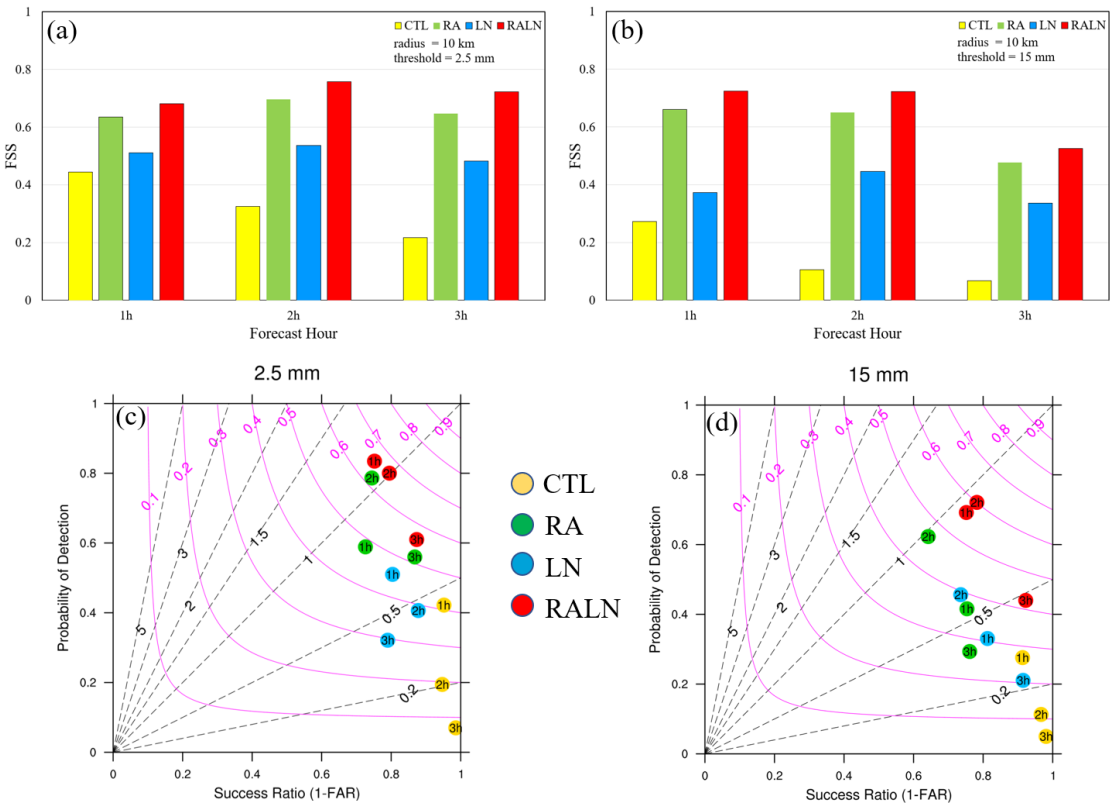

Fig. 7 (a-b) FSS of the hourly accumulated precipitation and (c-d) performance diagrams for each of the first three forecast hours with thresholds of 2.5 mm (left column) and 15 mm (right column) for the CTL (yellow), RA (green), LN (blue) and RALN (red) experiments initialized at 2000 on 13 July 2017. The results are shown for a neighborhood radius of 10 km. In the performance diagrams, the horizontal axis represents the success ratio (SR), the vertical axis represents the probability of detection (POD), the magenta lines represent the critical success index (CSI), the black dashed lines represent the frequency bias (FR), and the numbers inside the solid circles represent the forecast hour

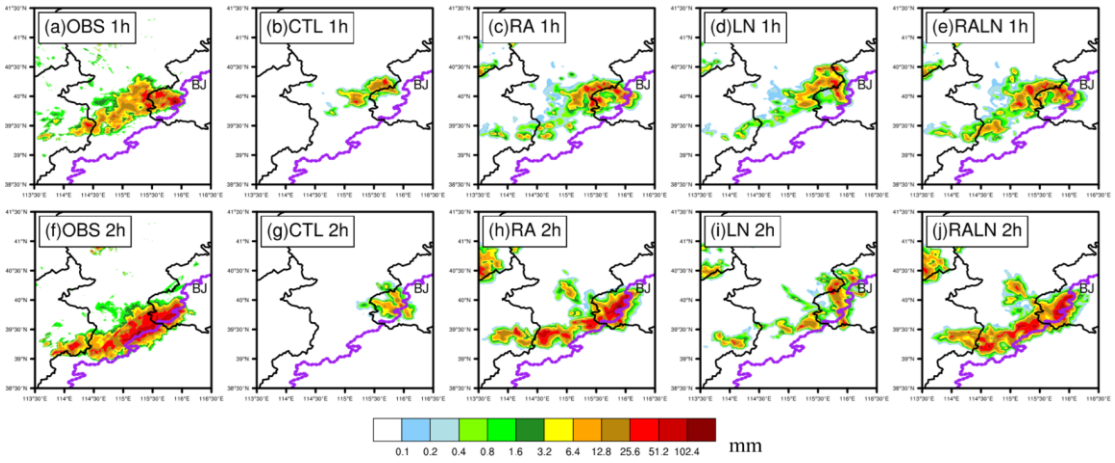

Fig. 8 Hourly accumulative precipitation (color, unit: mm) during the (a-e) 1st and (f-j) 2nd forecasting hour initialized at 2000 on 13 July 2017 for the radar QPE observations (1st column) and for the CTL (2nd column), RA (3rd column), LN (4th column) and RALN (5th column) experiments. The dashed purple line denotes the 400-m terrain elevation

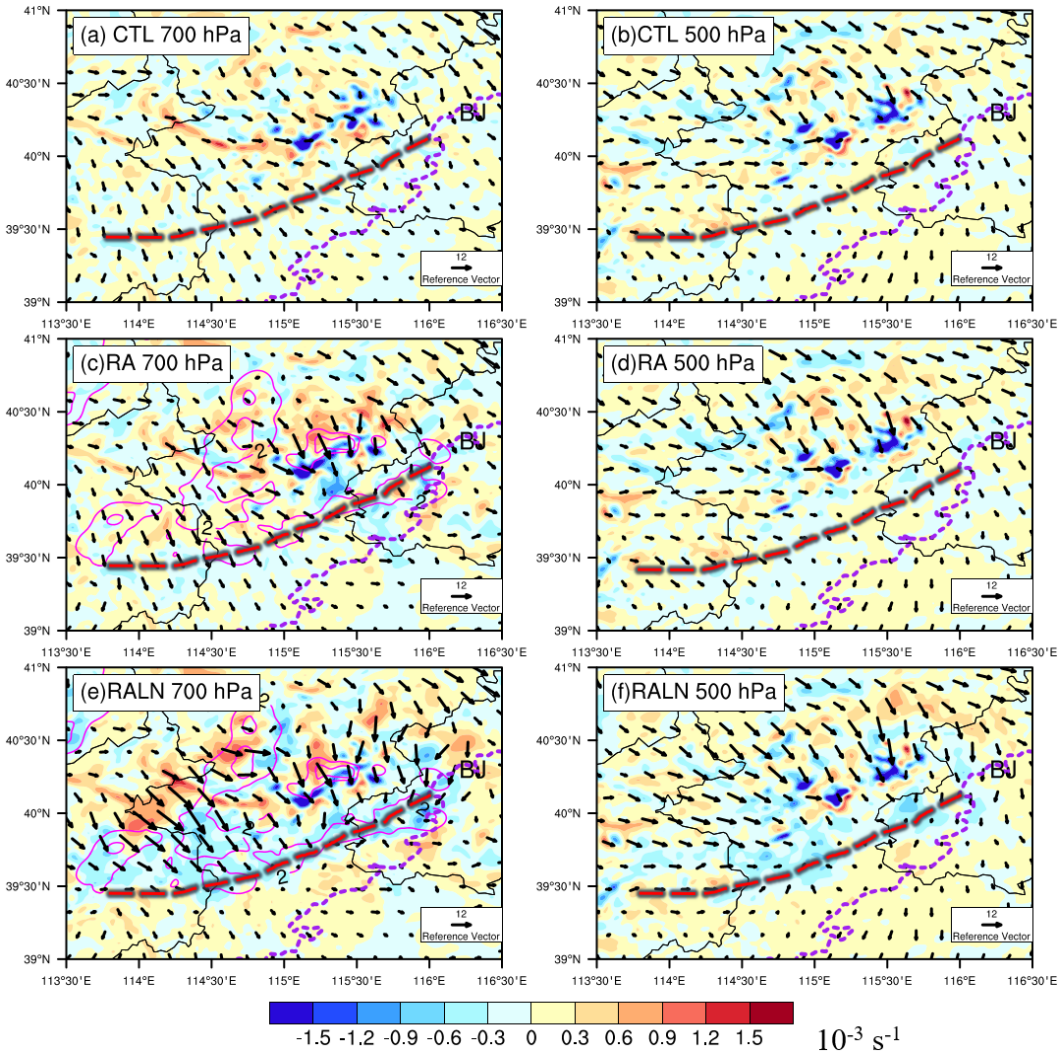

Fig. 9 Wind fields (vectors, the magnitude of the reference wind is 12 m s^{-1}) and wind convergence fields (color: 10^{-3} s^{-1}) for the (a-b) CTL, (c-d) RA and (e-f) RALN experiments at 700 hPa (left) and 500 hPa (right) at 2000 on 13 July 2017. The solid magenta contour lines (starting at 2 g kg^{-1} with an interval of 2 g kg^{-1}) denote the increments in the water vapor mixing ratios in RA and RALN. The long dashed red line denotes the location of the observed squall line, and the short purple line denotes the 400-m terrain elevation

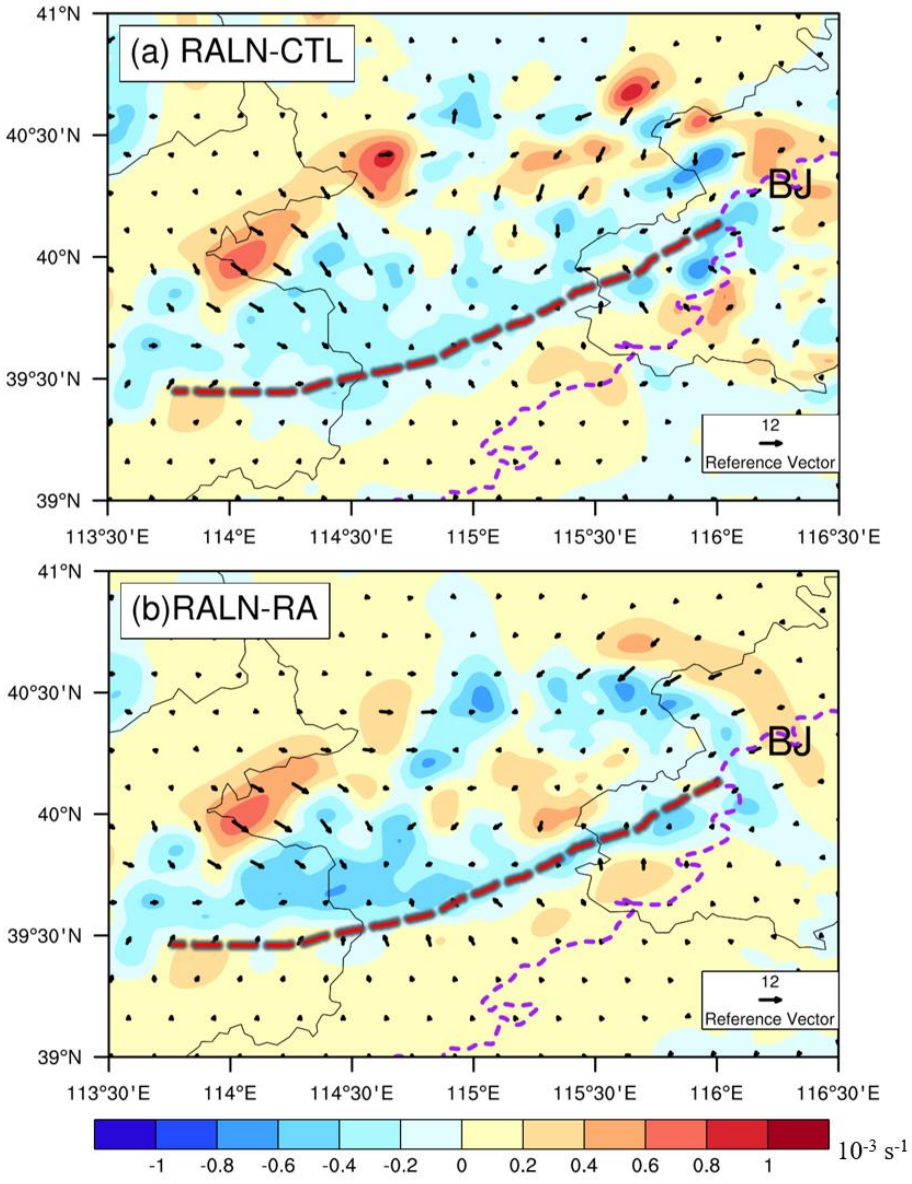

Fig. 10 Wind vector difference (vectors, the magnitude of the reference wind is 12 m s^{-1}) and convergence difference (color: 10^{-3} s^{-1}) between (a) RALN and CTL and (b) between RALN and RA at 700 hPa at 2000 on 13 July 2017. The long dashed red line denotes the location of the observed squall line, and the short purple line denotes the 400-m terrain elevation

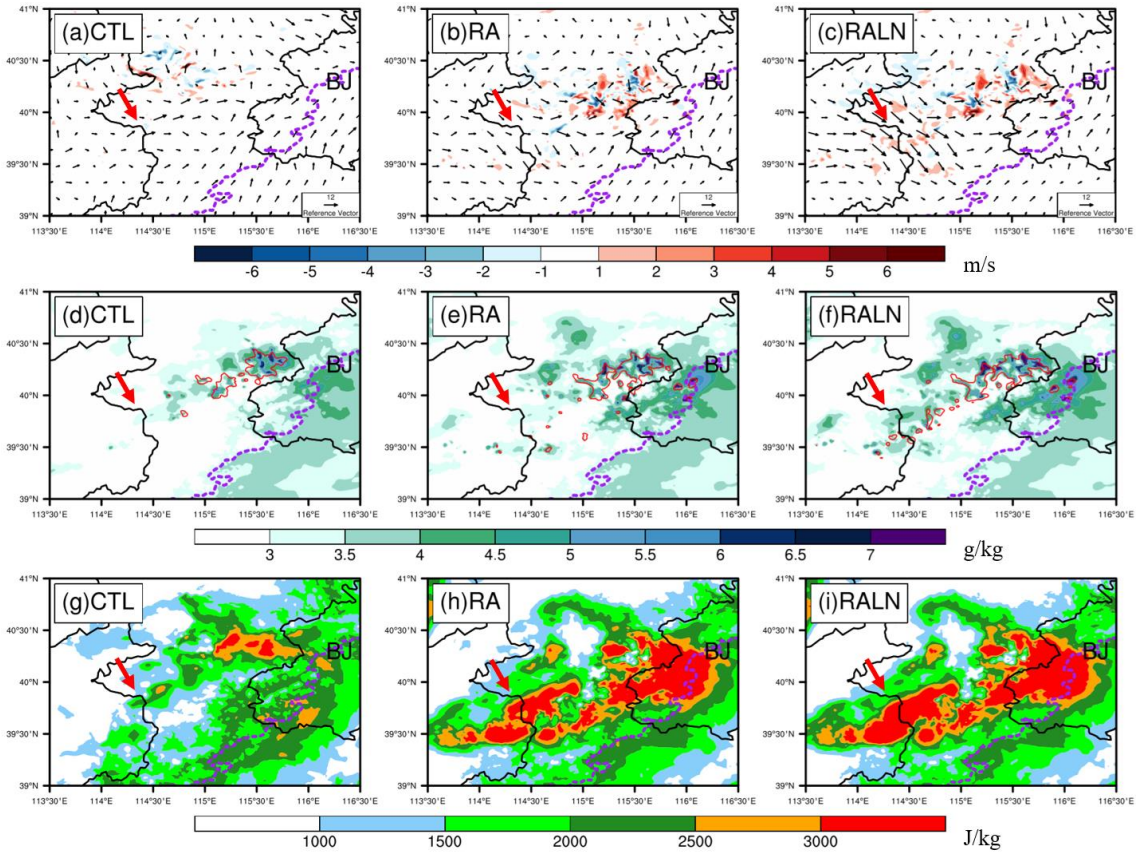

Fig. 11 (a-c) Vertical velocity *w* (color, unit: m s^{-1}) at 700 hPa superimposed by the 850-hPa horizontal wind field (vectors, the magnitude of the reference wind is 10 m s^{-1}), (d-f) layer-averaged water vapor mixing ratio (color, unit: g kg^{-1}) and rainwater mixing ratio (contour lines with values of 0.1 g kg^{-1}) between 700 hPa and 500 hPa, and (g-i) horizontal distribution of the maximum convective available potential energy (color, unit: J kg^{-1}) for the CTL (left), RA (center) and RALN (right) experiments at 2006 on 13 July 2017

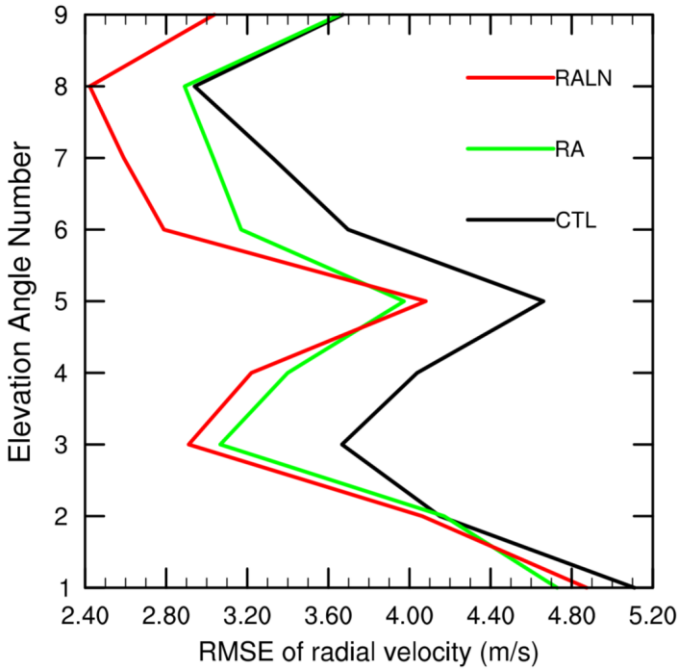

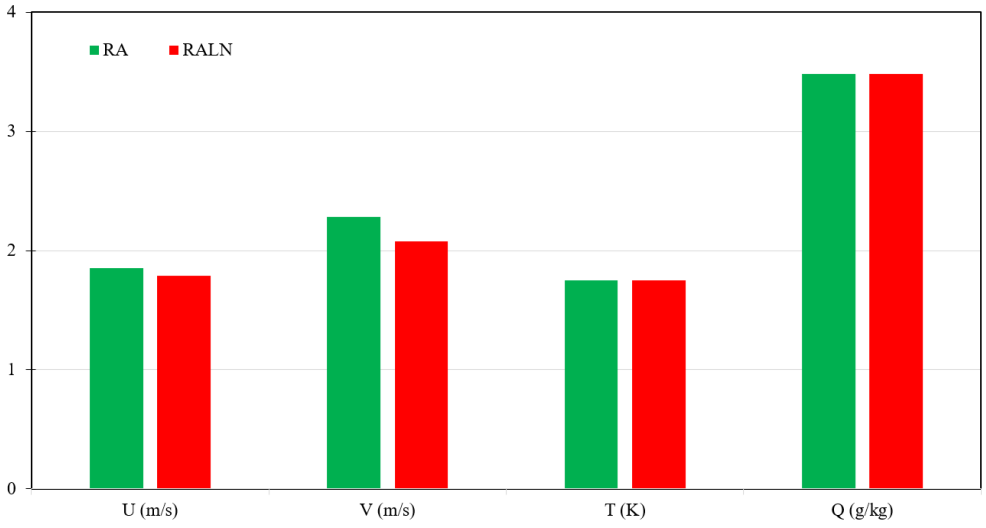

Fig. 12 RMSE of the (a) radial velocity verified against the Beijing Nanyuan Doppler radar observations and of the (b) wind components, temperature and water vapor mixing ratio compared with surface METAR observations

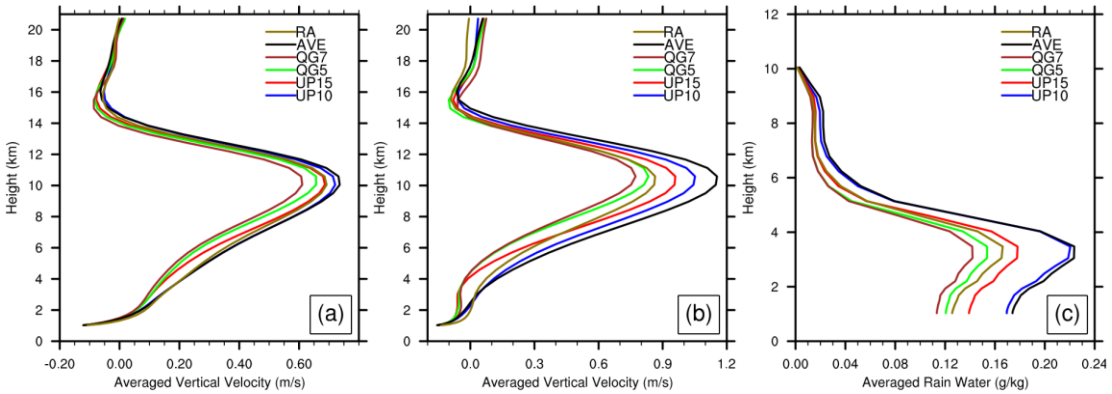

Fig. 13 Averaged vertical velocity profile (a) over the inner domain and (b) over lightning regions and the (c) rainwater mixing ratio profile over lightning regions for the 1st hour forecasts during 2000-2100 on 13 July 2017

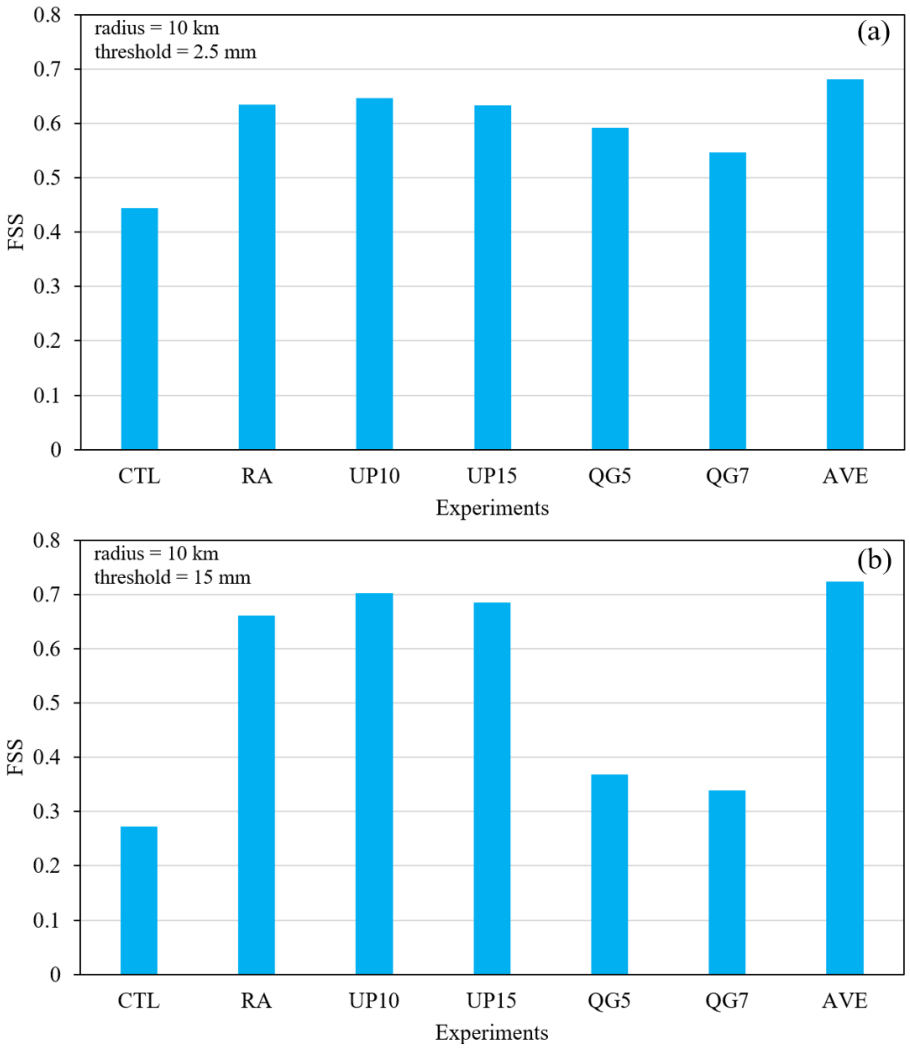

1183

1184 Fig. 14 FSS of the 1st hour accumulated precipitation forecasts during 2000-2100 on

1185 13 July 2017 with thresholds of (a) 2.5 and (b) 15 mm for all sensitivity experiments

1186

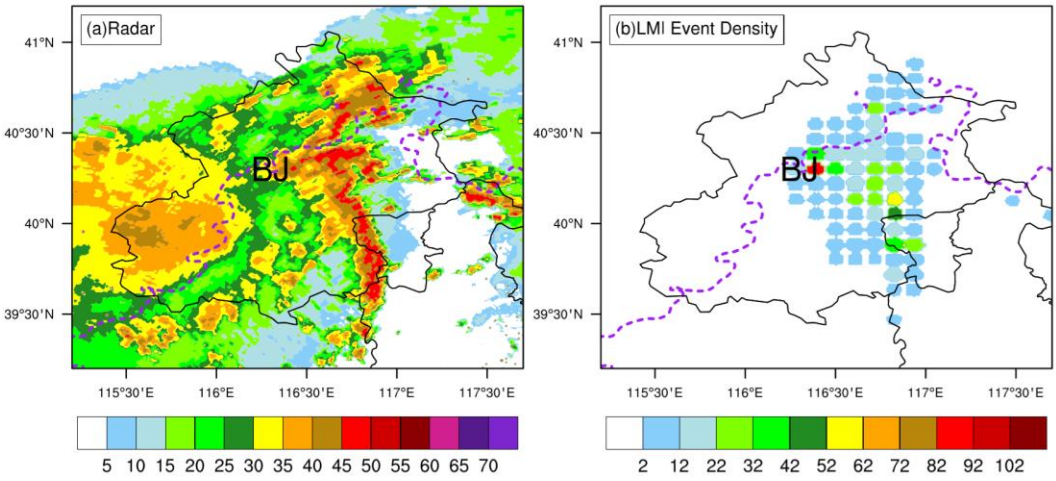

1187

1188 Fig. 15 (a) Composite radar reflectivity (unit: dBZ) at 0400 on 16 July 2018 and (b)

1189 LMI lightning event density (unit: 15 min^{-1}) from the LMI between 0345 and 0400

1190

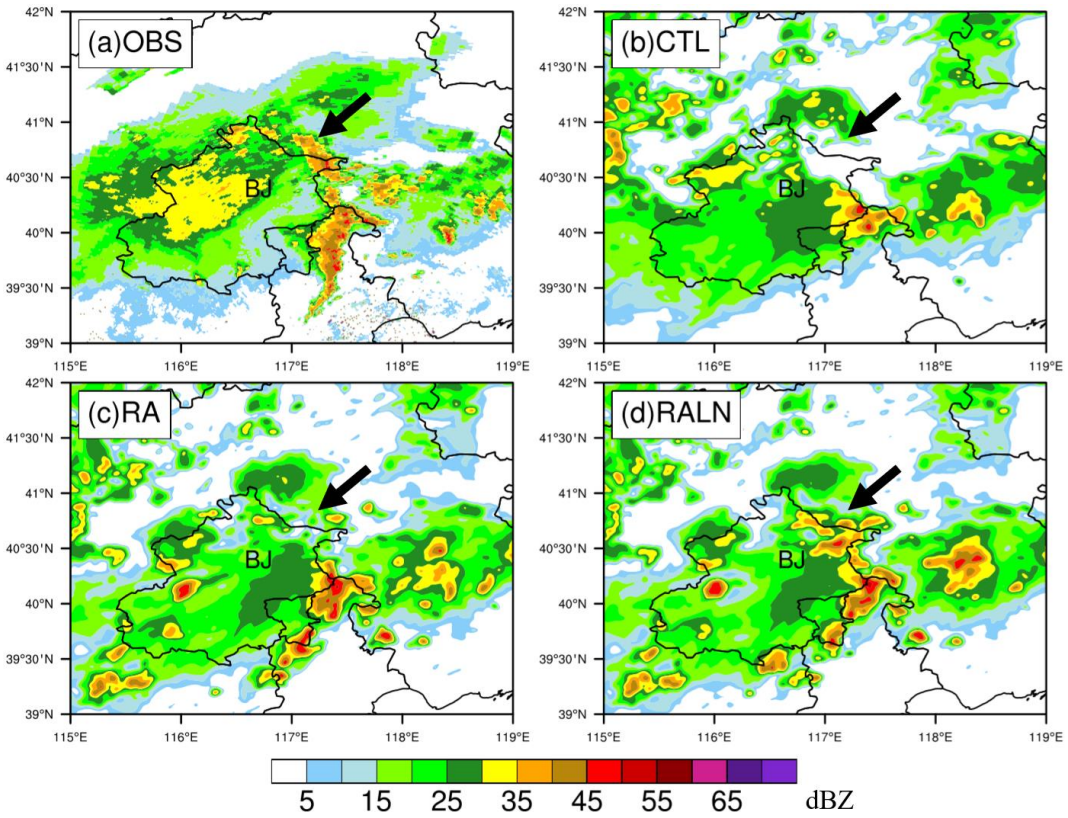

Fig. 16 Composite radar reflectivity (colors, unit: dBZ) of the (a) radar observations (OBS) and the (b) CTL, (c) RA, and (d) RALN experiments at 0500 on 16 July 2018

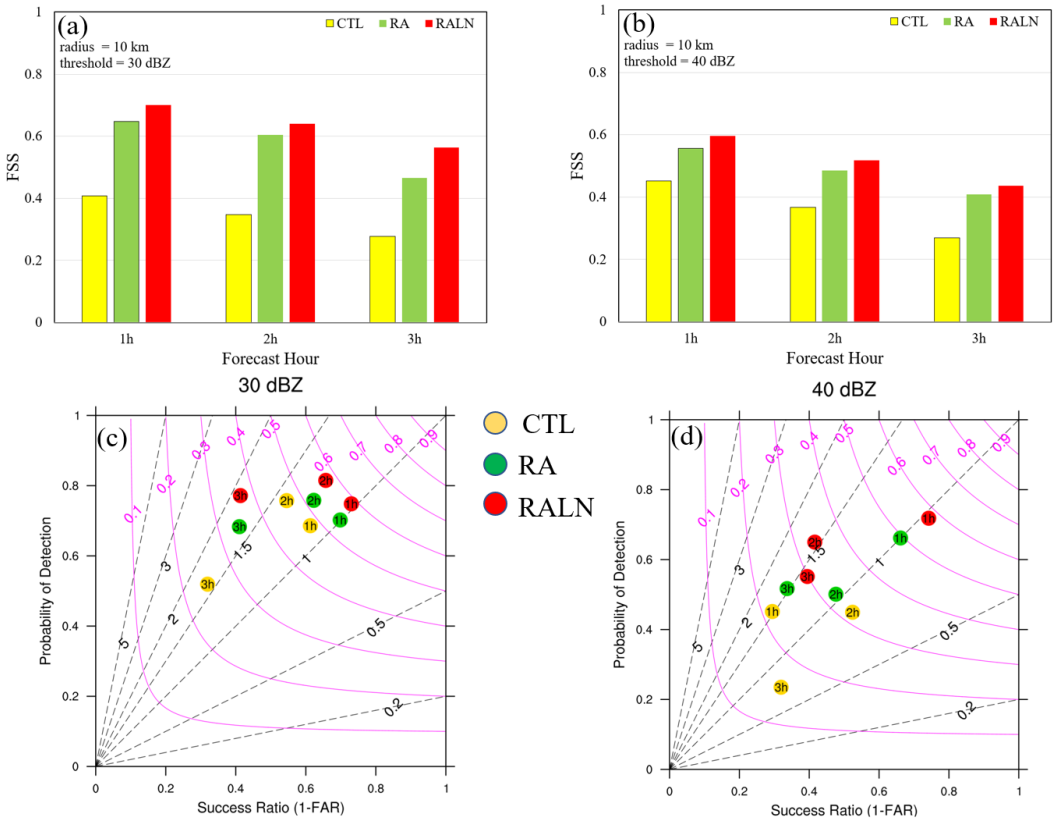

Fig. 17 Same as Fig. 7 but for the composite reflectivity fields initialized at 0400 on 16 July 2018 relative to radar observations with thresholds of 30 dBZ (left column) and 40 dBZ (right column)

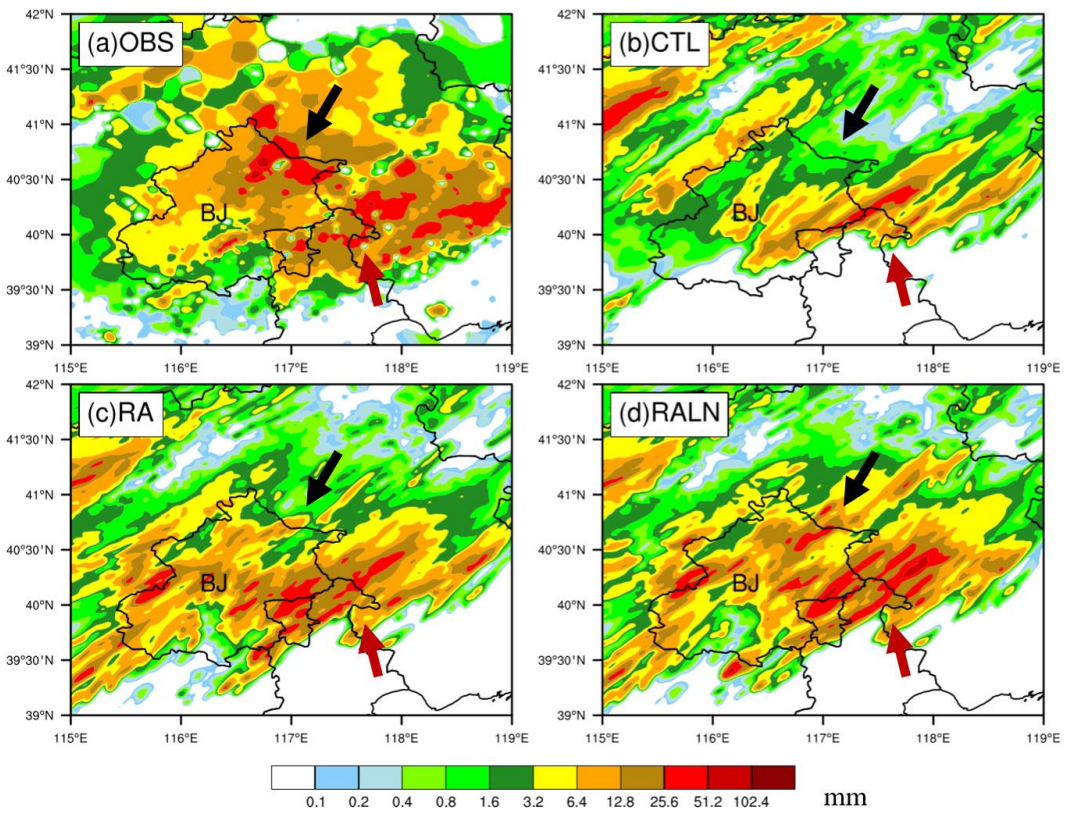

Fig. 18 Three-hour accumulative precipitation forecasts (color, unit: mm) initialized at 0400 on 16 July 2018 for (a) the radar QPE observations and for the (b) CTL, (c) RA and (d) RALN experiments

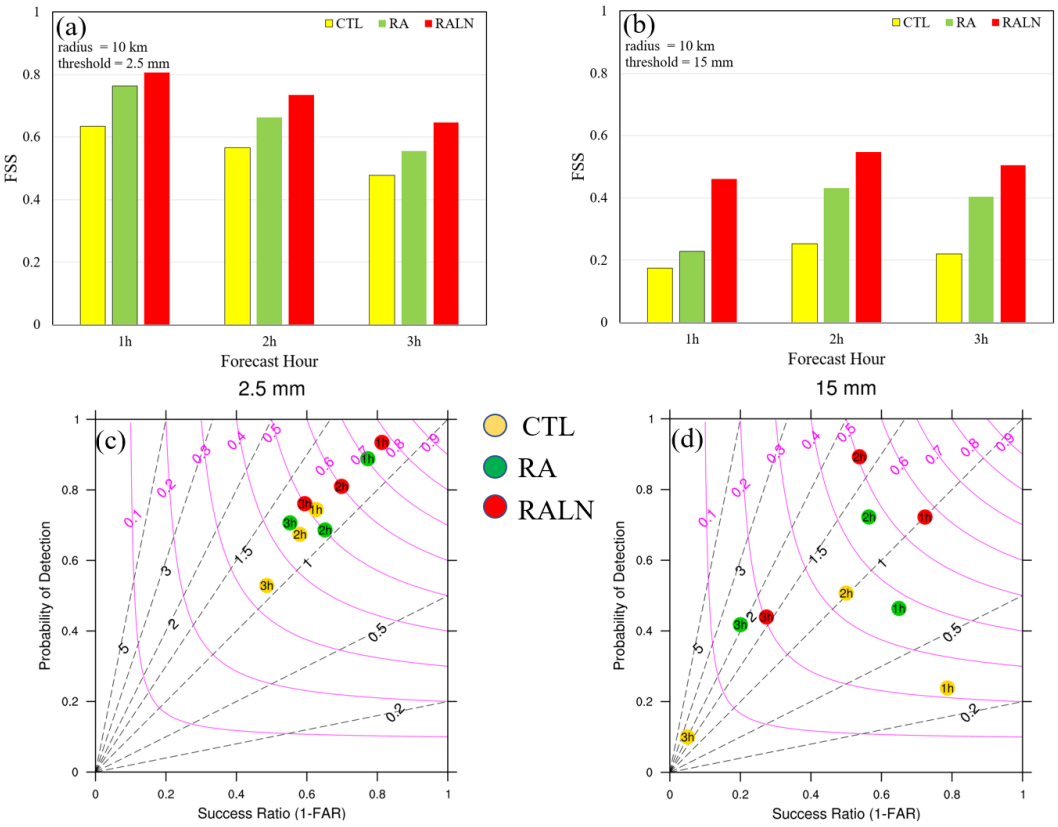

Fig. 19 Same as Fig. 7 but for the hourly accumulated precipitation initialized at 0400 on 16 July 2018 relative to radar observations with thresholds of 2.5 mm (left column) and 15 mm (right column)